EUROPEAN COMMISSION
Community Research

SEVENTH FRAMEWORK PROGRAMME

ARCHER

Collaborative Project (CP)

Co-funded by the European Commission under the
Euratom Research and Training Programme on Nuclear
Energy within the Seventh Framework Programme

Grant Agreement Number : 269892

Start date : 01/02/2011 Duration : 48 Months
www.archer-project.eu

Archer
Advanced Reactor
for Cogeneration of
Heat & Electricity-R&D

Validation of RANS and LES CFD approaches for dust behaviour in pebble beds

Authors : JAYARAJU Santhosh (NRG)

ARCHER - Contract Number: 269892
Advanced High-Temperature Reactors for Cogeneration of Heat and Electricity R&D
EC Scientific Officer: Dr. Panagiotis Manolatos

Document title	Validation of RANS and LES CFD approaches for dust behaviour in pebble beds
Author(s)	JAYARAJU Santhosh
Number of pages	48
Document type	Deliverable
Work Package	WP 23
Document number	D23.52
Issued by	NRG
Date of completion	16/01/2015
Dissemination level	Confidential, only for members of the consortium (including the Commission Services).

Summary

The main objective for NRG within the ARCHER project is to perform Computational Fluid Dynamics (CFD) modeling of graphite dust transport and deposition for a (V)HTR. This objective is achieved in the following two steps. ? Generic validation of Reynolds Averaged Navier Stokes (RANS) and Large Eddy Simulation (LES) CFD approaches. ? Pebble bed specific validation of RANS CFD approach. The generic validation of RANS and LES CFD approaches is addressed in the first deliverable D23.51 [1]. The present deliverable D23.52 concerns the application of this model to perform pebble-bed specific validation. The contents of the present deliverable are organized as follows: Chapter 2 provides general introduction to dust in HTR?s followed by a short summary of what was done in the previous deliverable D23.51. A description of what is done in the present deliverable D23.52 as a continuation of the previous work is also provided. Chapter 3 discusses generic validation analyses for cases where quantitative experimental reference data are available. In Chapter 4, the particle transport and deposition in three different pebble bed geometry configurations are investigated.

Approval

Date	By
17/01/2015	Karl VERFONDERN
20/01/2015	Norbert KOHTZ
20/01/2015	Steven KNOL

Distribution list

Name	Organisation	Comments
P. Manolatos	EC DG RTD	Through the EC participant portal
All beneficiaries	ARCHER	Through the private online workspace

Validation of RANS CFD approach for dust behavior in pebble beds

Santhosh Jayaraju

NRG-2.2902/14.130123/C&S/STJ/np
December 8, 2014

ARCHER Deliverable 23.52

author :	Santhosh Jayaraju	reviewed :	Arnè Siccama
36 pages		approved :	Ferry Roelofs

Contents

1 Summary

The main objective for NRG within the ARCHER project is to perform Computational Fluid Dynamics (CFD) modeling of graphite dust transport and deposition for a (V)HTR. This objective is achieved in the following two steps.

- Generic validation of Reynolds Averaged Navier Stokes (RANS) and Large Eddy Simulation (LES) CFD approaches.
- Pebble bed specific validation of RANS CFD approach.

The generic validation of RANS and LES CFD approaches is addressed in the first deliverable D23.51 [1]. The present deliverable D23.52 concerns the application of this model to perform pebble-bed specific validation. The contents of the present deliverable are organized as follows:

Chapter 2 provides general introduction to dust in HTR's followed by a short summary of what was done in the previous deliverable D23.51. A description of what is done in the present deliverable D23.52 as a continuation of the previous work is also provided. *Chapter 3* discusses generic validation analyses for cases where quantitative experimental reference data are available. In *Chapter 4*, the particle transport and deposition in three different pebble bed geometry configurations are investigated.

2 Introduction

A very high temperature (VHTR) or high temperature gas cooled reactor (HTGR) is under consideration as a fourth generation advanced nuclear reactor. The reactor uses graphite as a moderator and helium gas as a coolant. Because of high core outlet temperature, high thermal efficiency is achieved in these types of reactors. Moreover, the VHTR can be designed such that there is no need for active safety systems to remove the decay heat from the reactor core as it is designed to lose heat by itself from thermal radiation and natural circulation. A number of experimental and prototype reactors have been built and operated in the past. Examples of high temperature reactors are the Dragon reactor (United Kingdom), the Peach Bottom reactor (United States of America), AVR and THTR 300 (Germany) and the reactor at Fort St. Vrain (United States of America). At present, there are experimental reactors under operation in Japan (HTTR) and China (HTR-10). Apart from this, two full scaled HTGRs, the two-module plant HTR-PM, are under construction in China.

The core design in these types of reactors is generally based on prismatic or pebble bed arrangement. In a typical pebble bed reactor, the reactor core consists of randomly stacked pebbles. Typically there are several hundred thousands of them in the core. These pebbles are primarily made of graphite and contain uranium dispersed in coated sand-size grains throughout the pebble. One of the sources of dust production is due to the abrasion of randomly stacked graphite pebbles. The generated dust is essentially composed of carbonaceous compounds, fission and activation products. In a 400 MW thermal pebble-bed HTR, abraded dust is anticipated to be in the range of 30-100 kg/yr [2]. The dust is eventually carried by helium gas through the primary circuit and gets deposited in its main components such as the main pipes systems, the heat exchangers (steam generators, intermediate heat exchangers or recuperators) and turbo-machinery if applicable. Remobilisation of dust deposited in the primary system is identified as one of the foremost concerns during a depressurisation accident [3]. Hence, accurate prediction of dust transport and deposition is an important step in the design of this type of reactors.

The first deliverable D23.51 was related to generic validation for the RANS and LES CFD approaches to predict the particle transport and deposition. Detailed literature review was performed to collect and evaluate the available experimental and Direct Numerical Simulation (DNS) data pertaining to the particle deposition validation. In case of RANS modelling, several uncertainties regarding the near-wall modeling were addressed. A robust and well validated RANS model coupled with a specific near-wall correlation was proposed for the accurate particle transport and deposition predictions. Additionally, the capability of a more advanced model such as the LES was validated by performing two test cases.

The present deliverable D23.52 concerns the application of the validated model presented in D23.51 to perform pebble-bed specific validation. Due to the geometric and measurement complexities, random pebble bed experiments performed in the literature have a very limited amount of available data. The recent experiments from [4] provides good quantitative predictions of particle deposition behavior in a randomly stacked pebble beds, however, no explicit data is available to translate the random pebble bed arrangement into a CAD model. Due to such limitations, it becomes difficult to directly apply the proposed model in D23.51 to predict particle transport and deposition in complex domains of random pebble beds. Hence, the following approach is taken to built confidence in the proposed model:

Generic validation

- Validate the proposed model by applying it to simple cases such as duct flow, stright pipe flow and bend pipe flow where experimental data are available for particle deposition.
- Validate the proposed model by applying it to simple cases such as flow over single sphere and flow over array of spheres where experimental data are available for particle deposition. These validation cases more resemble the complex flow which can be expected in pebble-beds.

Pebble bed specific validation

- Apply the proposed model to two structured pebble beds in face cubic centered (FCC) arrangements. From fluid flow point of view, recent q-DNS and LES computations of Shams et al. [5],[6],[7] allow more in-depth validation of the flow structures. From particle transport and deposition perspective, these cases enable us to systematically demonstrate the deposition patterns in such arrangements.
- Finally, apply the proposed model to a a randomly stacked pebble bed configuration to demonstrate the expected deposition patterns in such an arrangement.

3 Computational approach

The analyses are done through the CFD software *ANSYS Fluent 14*. The fluid phase is treated as incompressible. A pressure based solver in steady state conditions is applied. Turbulence is modeled through a standard $k - \epsilon$ model with the so-called enhanced wall treatment (*ANSYS Fluent 14*). Second order upwind scheme is selected for spatial discretization.

Based on the physical properties of dust measured in AVR, their estimated behavior in different regions of an HTR, and on the mathematical modeling effort required, there are certain reasonable assumptions made to describe the dust aerosol transport and deposition in a HTR. The major assumptions for the present work are as follows.

- The particle is taken to be spherical.
- The ratio of the particle to the fluid density is assumed to very large.
- Air flow is not affected by the presence of particles and effects of the particle on turbulence are neglected i.e. one way coupling is assumed.
- The particle phase is dilute i.e. the volume loading of the particles is assumed to be negligibly small.
- Particle-particle interactions are neglected. The particle rotational and thermophoretic forces are assumed to be zero.

The particle transport modeling is based on the continuous random walk (CRW) model. Within this approach, the particle deposition modeling is divided into two regions namely, the boundary layer region with strong anisotropic turbulence and bulk flow region with isotropic turbulence. The model is based on a Langevin equation. The Langevin equation takes different forms depending on the particle location which could be in the boundary layer or in the bulk region. In the **boundary layer region**, the normalized Langevin equation for streamwise, wall-normal and spanwise directions are given by:

$$d\left(\frac{u'}{u_{rms}}\right) = -\left(\frac{u'}{u_{rms}}\right).\frac{\Delta t}{\tau_L} + \sqrt{\frac{2}{\tau_L}}.d\xi_x \tag{1}$$

$$d\left(\frac{v'}{v_{rms}}\right) = -\left(\frac{v'}{v_{rms}}\right).\frac{\Delta t}{\tau_L} + \sqrt{\frac{2}{\tau_L}}.d\xi_y + \frac{\partial v_{rms}}{\partial y}.\frac{\Delta t}{1 + Stk} \tag{2}$$

$$d\left(\frac{w'}{w_{rms}}\right) = -\left(\frac{w'}{w_{rms}}\right).\frac{\Delta t}{\tau_L} + \sqrt{\frac{2}{\tau_L}}.d\xi_z \tag{3}$$

where, $u^{'}$, $v^{'}$ and $w^{'}$ are the fluid fluctuating velocity components in streamwise, wall-normal and spanwise directions. u_{rms}, v_{rms} and w_{rms} are the corresponding RMS velocity components. x, y and z are the coordinates in x, y and z directions. ξ_x, ξ_y and ξ_z are the Gaussian random numbers with zero mean and variance dt.

In the above equation, Stk is a particle Stokes number, which is the ratio of particle relaxation time to the Lagrangian time scale and is given by:

$$Stk = \frac{\tau_p}{\tau_L}. \tag{4}$$

The last term in RHS of Eq. 2 is the mean drift correction term, which is added to avoid the un-physical migration of small inertial particles towards the boundary layer. [8] indicated that neglecting this term lead to overestimation of the particle deposition.

In the **bulk flow region**, the following equations for the normalized Langevin equations are solved for streamwise, wall-normal and spanwise directions:

$$d\left(\frac{u^{'}}{u_{rms}}\right) = -\left(\frac{u^{'}}{u_{rms}}\right).\frac{\Delta t}{\tau_L} + \sqrt{\frac{2}{\tau_L}}.d\xi_x + \frac{1}{3u_{rms}}.\frac{\partial k}{\partial x}.\frac{dt}{1+Stk} \tag{5}$$

$$d\left(\frac{v^{'}}{v_{rms}}\right) = -\left(\frac{v^{'}}{v_{rms}}\right).\frac{\Delta t}{\tau_L} + \sqrt{\frac{2}{\tau_L}}.d\xi_y + \frac{1}{3v_{rms}}.\frac{\partial k}{\partial y}.\frac{dt}{1+Stk} \tag{6}$$

$$d\left(\frac{w^{'}}{w_{rms}}\right) = -\left(\frac{w^{'}}{w_{rms}}\right).\frac{\Delta t}{\tau_L} + \sqrt{\frac{2}{\tau_L}}.d\xi_z + \frac{1}{3w_{rms}}.\frac{\partial k}{\partial z}.\frac{dt}{1+Stk} \tag{7}$$

where, k is the turbulent kinetic energy.
Based on the validation work in D23.51, the following conclusions can be drawn about the model parameters:

- Several correlations exist in the literature to model the near-wall anisotropy in the fluid phase. Carefully choose a correlation which is accurately representing the DNS data. In D23.51, it is shown that both the Drebeen et al. and the Wang and James correlations are showing good fits to the DNS data. Hence, either of these models can be used.

- For y^+ <30, the DNS data showed no considerable sensitivity for a range of Re_τ. Hence, near-wall corrections can be applied up to y^+ of 30.

- A y^+ value of 30 is recommended as a cut-off below which the near-wall anisotropy effects should be considered. Applying anisotropy cut-off below y^+ 30 leads to over-estimation of particle deposition velocity in a certain range of particle relaxation times.

- The values of 2, 6 and 10 for τ_L^+ in the region below y^+ of 5 have no considerable effect on the deposition velocity predictions.

4 Generic Validation

In the present chapter numerical simulations of particle deposition in four different flow cases are discussed. Background, set-up of simulations and results are subjects of the discussions.

In *Section 4.1* particle deposition in a 2D horizontal channel is discussed, this is followed in *Section 4.2* by a discussion on particle deposition in a vertical straight pipe. After this, in *Section 4.3* deposition in a 90° bend pipe is discussed. The last case in *Section 4.4* concerns the deposition on spheres.

4.1 2D channel

This section deals with particle deposition in a horizontal two-dimensional channel.

4.1.1 Experimental data

Barth et al. [9] performed particle deposition experiments in an open air horizontal channel. The experimental facility is as shown in Fig. 1. Aerosols are injected through the aerosol generator upstream. The flow is let to develop in the formation zone. The measurements are performed in the square duct test section as shown. Deposition was investigated for micron-sized fluid particles in the range of d_p = [2.5, 3.8, 4.5, 5.8] μm. The fluid-to-particle density ratio was S = 760. Particles were sampled using particle size spectrometry and surface deposited particles were detected by means of optical microscopy. Comparison of particle deposition velocities showed good agreement with Wood's correlation [10].

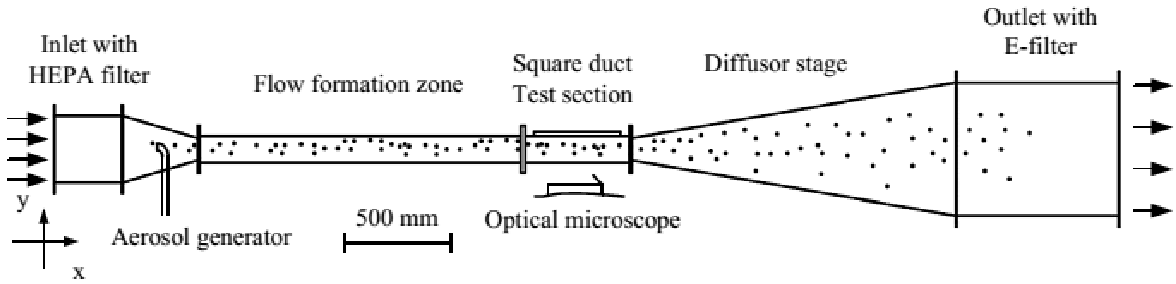

Figure 1 Barth et al. [9] experimental facility.

4.1.2 CFD domain

The computational domain and mesh used in the 2D channel case are based on the work of Tian and Ahmadi [11].

The channel under investigation is 0.02 m wide and 0.4 m long. The domain is meshed with hexahedral cells. Cells in streamwise and lateral direction are 0.5 mm long. In the near-wall region, the first grid point is located at 0.05 mm off the wall and cell height increases with a stretching ratio of 1.2. The mesh is shown in Figure 2. Tian and Ahmadi [11] have shown that this grid resolution is sufficient to obtain grid-independent results for the flow field and particle deposition.

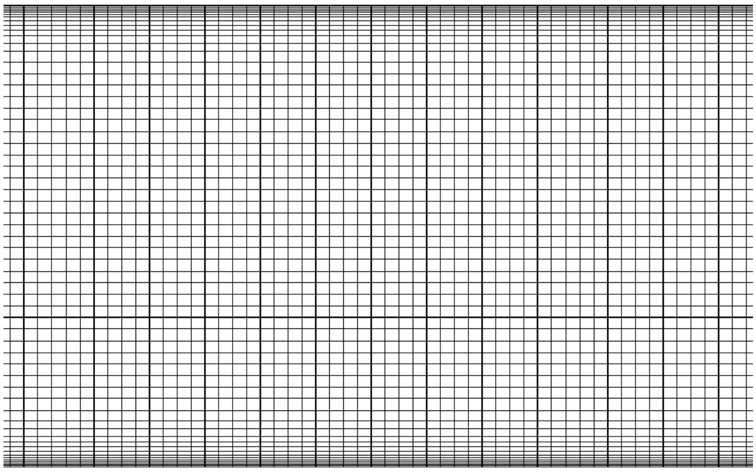

Figure 2 Mesh view of 2D channel case.

4.1.3 Flow parameters

Air is used as carrier fluid with a density ρ = 1.2 kg/m^3 and viscosity of μ = 1.8×10^{-5} Ns/m^2. Four different flow rates corresponding to u_τ = [0.08, 0.21, 0.33, 0.49] m/s are studied. Gravity acts in wall-normal direction of bottom wall.

4.1.4 Particle parameters

The particle diameters and fluid-to-particle density ratio are taken similar to Barth et al. [9]. Particles are injected halfway the length of the channel where the flow is fully developed. The particles diameters are 2.5, 3.8, 4.5 and 5.8 [μm], injected by uniformly distributing them between $0 < \Delta y^+ < 30$. For each particle diameter 3,000 particles are injected. In cases where the number of injected particles was increased to 10,000 and 30,000 no considerable effect on the deposition statistics was found.

The non-dimensional particle relaxation time is used to express the particle size:

$$\tau^+ = \frac{S d_p^2 u_\tau^2}{18\nu^2} C_c \tag{8}$$

Here, $S = \frac{\rho_p}{\rho_f}$ is the particle-to-fluid density ratio, d_p the diameter of the particles, u_τ the friction velocity, ν the kinematic viscosity of the carrier fluid. C_c is the Cunningham slip factor, defined as:

$$C_c = 1 + \frac{2\lambda}{d_p}\left(1.257 + 0.4e^{\frac{1.1d_p}{2\lambda}}\right) \quad (9)$$

The particle deposition velocity is calculated using:

$$u_d^+ = \frac{N_d/t_d^+}{N_0/y_0^+} \quad (10)$$

N_d is the number of deposited particles on the bottom wall downstream the injection, N_0 is the total number of injected particles, y_0^+ is the non-dimensional height from the wall over which the particles are injected, t_d^+ is the non-dimensional average time in which the particles have deposited.

4.1.5 Results

Figure 3 shows the particle deposition velocities for four different friction velocities. In this figure the experimental results of Barth et al. [9] and Wood's correlation [10] are shown as well. From the figure it can be concluded that the obtained particle deposition velocities are in good agreement with both the experimental results and Wood's correlation for low Reynolds number (low u_τ). For higher Reynolds numbers (higher u_τ) computational results are in better agreement with Wood's correlation rather than Barth experimental results. In the previous deliverable D23.51, one set of RANS simulations was done using the default particle tracking models available in Fluent. The results were indeed poor when compared to the CRW model results presented here.

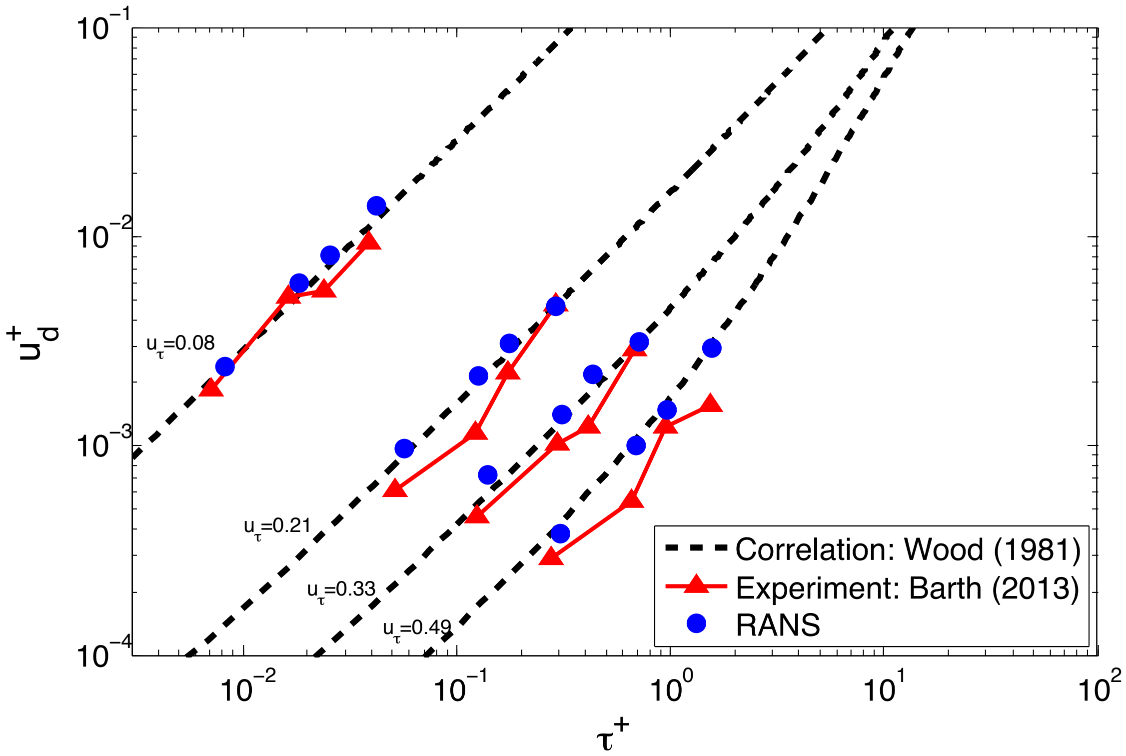

Figure 3 Deposition velocity u_d^+ in a 2D horizontal channel for four different friction velocities versus particle relaxation time τ^+. Results of current simulations compared with the experimental data [9] and Wood's correlation [10].

4.2 Straight pipe

In this section, particle deposition in a straight vertical pipe is discussed.

4.2.1 Experimental data

Liu and Agarwal [12] conducted experiments in a straight pipe. The experimental facility is as shown in Fig. 4. The mono-disperse aerosols which passes through the neutralizer is further diluted by the secondary dilution air. The mixture then enters the transition pipe through the plenum chamber. The deposition of olive oil particles of 1.4-21 μm is measured in the deposition pipe region. The deposition pipe region is a vertical glass pipe with a diameter of 1.27 cm and a length of 1 m in the streamwise direction. Deposition data is presented for a section of 0.508 m (between 0.255 m and 0.763 m) where the flow is fully developed and far enough from the outlet. The gas velocity is 12 m/s. A scheme of the experimental facility is shown in Figure 4.

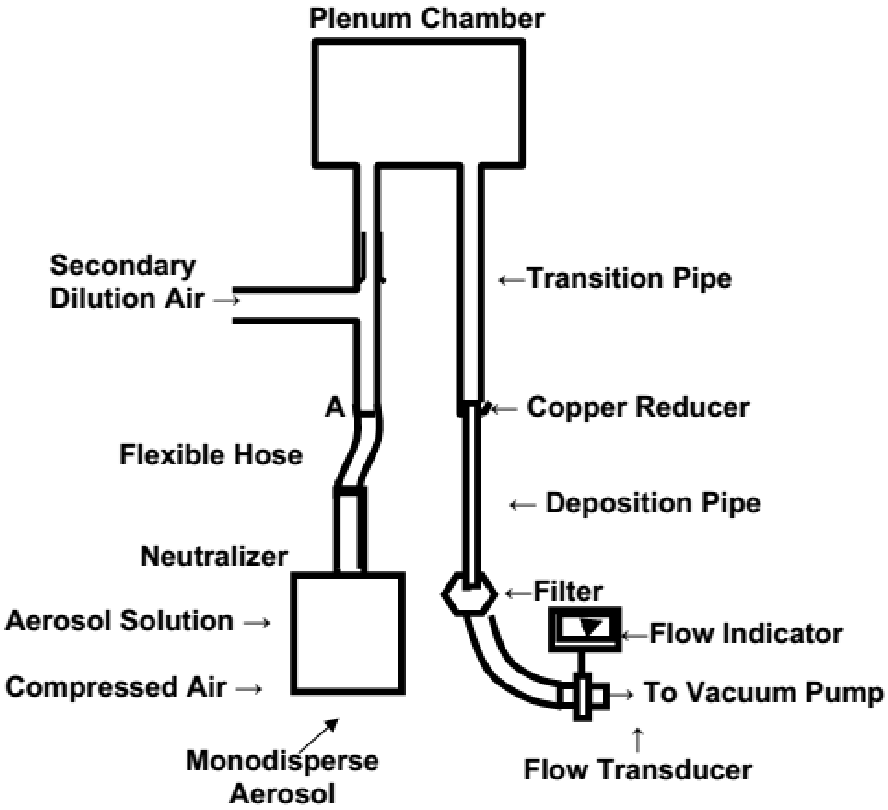

Figure 4 Liu and Agarwal [12] experimental facility.

4.2.2 CFD domain

The CFD domain replicates the experiments of Liu and Agarwal [12]. Mesh settings are similar to Dehbi [13] who performed CFD simulations of a straight channel replicating the experiment of Liu and Agarwal [12]. A 3D hexahedral mesh was generated in which the near-wall cells have $y^+ < 1$ and in the boundary layer 30 cells are present. The injected particles have a density of ρ_p = 920 kg/m^3. A total number of 10,000 particles is injected. Simulations with larger numbers showed no change in the deposition rate [13]. The results of Dehbi [13] agree with the experimental data of Liu and Agarwal and with the empirical correlation of McCoy and Hanratty [14].

4.2.3 Flow parameters

The carrier fluid is air with a density of ρ = 1.225 kg/m^3 and viscosity of μ = 1.8669 $\times$ 10^{-5} Ns/m^2. The flow rate respect the experimental condition of Reynolds number $Re = 10\,000$. Gravity acts in direction $-y$.

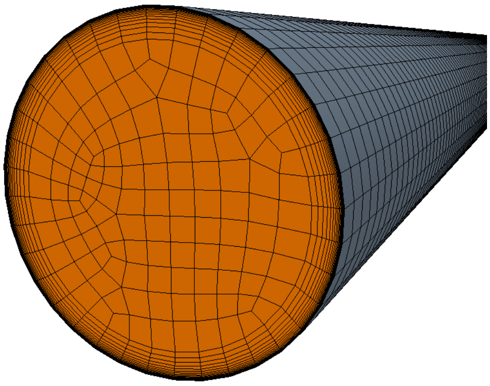

Figure 5 Mesh of straight pipe case.

4.2.4 Particle parameters

Particles with diameters in the range of 2-50 μm are injected with a density similar to Dehbi [13]. For each particle diameter about 10,000 particles - similar to Dehbi [13] - are injected at the inlet of the pipe. Particles that deposit in the region between 0.255 m and 0.763 m are counted as deposited particles.

Dimensionless particle deposition velocity is defined as:

$$u_d^+ = \frac{1}{4}\frac{D}{L}\frac{\bar{U}}{u^*}\ln\left(\frac{C_{in}}{C_{out}}\right) \tag{11}$$

where D and L are the pipe diameter and length, respectively, $\bar{U}$ the inlet velocity, u^* the friction velocity at the wall and the C's refer to the particle number concentrations.

4.2.5 Results

The particles are released in the part of the pipe where the flow is developed, as was mentioned before. In Figure 6.a the velocity magnitude at the entry region of the pipe is shown. The development of the flow field is visible. In the latter part of the pipe, the flow field is developed, see Figure 6.b. It reaches the maximum value of the velocity in the middle which is 14.2 $\frac{m}{s}$.

The turbulent kinetic energy in the developed region at the midplane of the pipe is shown in Figure 7. The turbulent kinetic energy is high in the boundary layer region where the gradients of the velocity magnitude occur due to the presence of the wall. Comparing Figures 6.b and 7.b it can be learned that the development of the turbulent kinetic energy is visible in a longer section than the development of the flow field. This underlines the need for injection of the particles well enough downstream of the inlet to prevent influences of the development of the flow field.

The non-dimensional deposition velocity u_d^+ versus the particle relaxation time τ^+ is shown in Figure 8. For

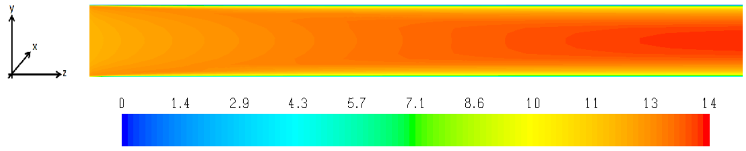

a Entry region

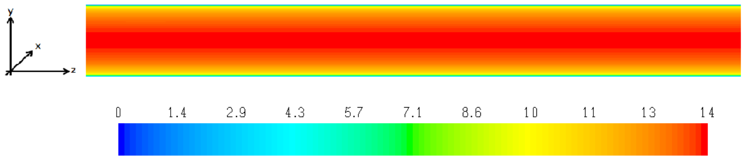

b Developed region

Figure 6 Velocity magnitude at midplane of the straight pipe m/s.

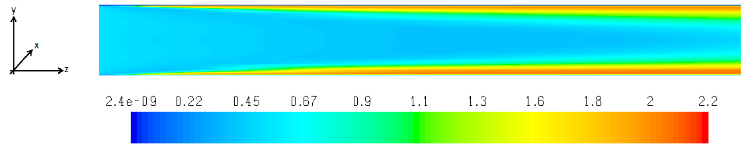

a Entry region

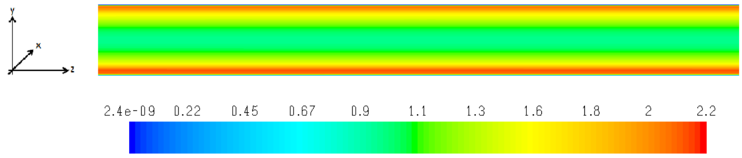

b Developed region

Figure 7 Turbulent kinetic energy at midplane of the straight pipe m^2/s^2.

comparison, the experimental results of Liu and Agarwal [12] are plotted as well as the empirical correlation of McCoy and Hanratty [14]. Also reported is the deposition efficiency result of the LES computation done by NRG which was presented in the previous deliverable D23.51. Obtained numerical results are close to the experimental results and follow the trends of the empirical correlation. Overall, the numerical trend of computational results is in good agreement with both the experimental data and the empirical correlation, in spite of the fact that the deposition velocity is slightly overestimated.

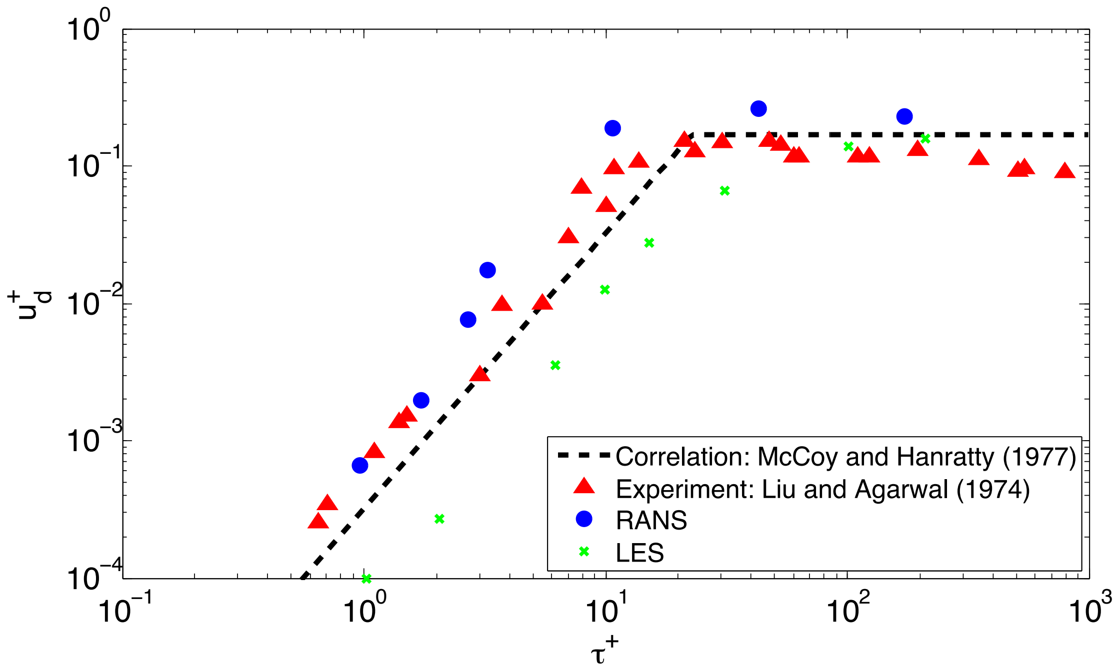

Figure 8 Non-dimensional deposition velocity u_d^+ in a vertical pipe versus particle relaxation time τ^+. Results of current simulation compared with the experimental data of Liu and Agarwal [12] and correlation of McCoy and Hanratty [14].

4.3 Bend pipe

Particle deposition in a 90° bend pipe is discussed in this section.

4.3.1 Experimental data

Pui et al. [15] conducted experiments on particle deposition in a 90 degrees bend pipe. The experimental facility is as shown in Fig. 9. The generated aerosol coming from the neutralizer enters the inflow section of the pipe which is horizontal. The deposition zone is at the end of this horizontal pipe which forms the 90 degree bend. After the bend, the pipe is directed downwards in the direction of gravity. Deposition with flow Reynolds numbers in the range of 100-10,000 were studied. Based on the experimental results, Pui et al. [15] derived an empirical relation that fitted the results. The experimental facility of Piu et al. is shown in 9.

In the flow case with Re = 10,000, the curvature ratio of the pipe varied between R_0 = 5.6 and R_0 = 5.7. The tube inner diameter (d) was 8.51 mm (for the cases with R_0 = 5.6) and 5.03 mm (for the cases with R_0 = 5.7). The curvature ratio R_0 is defined as ratio between pipe diameter (d) and twice the curvature radius (R_c), so $R_0 = \frac{d}{2*R_c}$

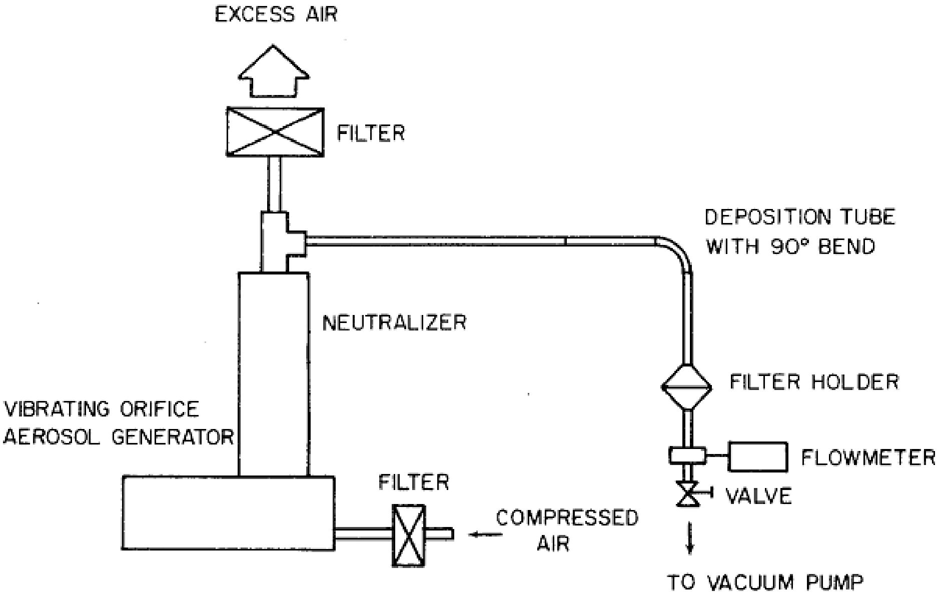

Figure 9 Pui et al. [15] experimental facility.

Particle dimensions are given in non-dimensional Stokes numbers. In the flow case with Re = 10,000, the Stokes numbers were in the range St = [0.27, 0.29, 0.46, 0.75, 0.84, 1.22 1.35], with the Stokes number defined as:

$$St = \frac{C\rho_p d_p^2 \bar{U}}{18\mu r} \tag{12}$$

with C a slip factor, ρ_p the particle density, d_p the particle diameter, $\bar{U}$ the bulk velocity, μ the fluid viscosity and r the radius of the pipe.

Deposition efficiency is defined as:

$$\eta = \frac{N_{dep}}{N_{tot}} \tag{13}$$

The efficiency η is given in %, N_{dep} is the number of deposited particles and N_{tot} the number of particles that exited the pipe.

4.3.2 CFD domain

The flow case Re = 10,000 with R_0 = 5.6 is replicated numerically. The CFD domain is based on Breuer [16] who replicated the experiment of Pui et al. [15]. The LES results obtained by Breuer [16] agree well with the experimental data and correlation of Pui et al. [15]. The inflow conditions are chosen such that a developed flow profile exists before the bend. The mesh, shown in Figure 10, is wall-resolved and contains about 1.5 $\times$ 10^5 cells.

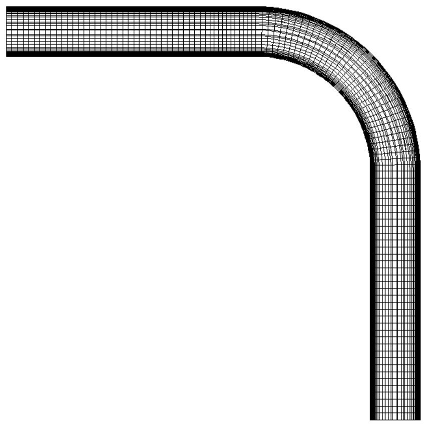

a

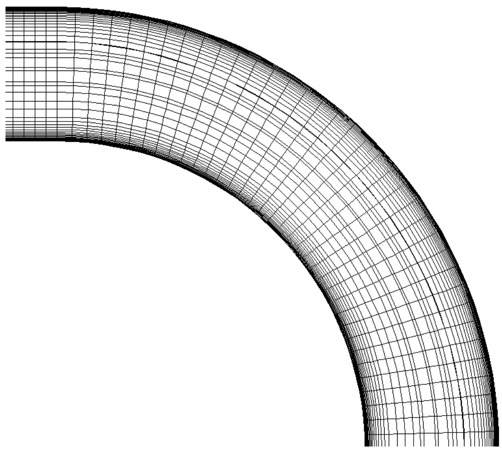

b

Figure 10 Mesh of bend pipe case: (a) whole domain; (b) detail of the bend.

4.3.3 Flow parameters

Air is used as carrier fluid with density ρ = 1.155 kg/m^3 and viscosity μ = 1.848 $\times$ 10^{-5} Ns/m^2. The inflow velocity is $\bar{U}$ = 8 m/s. Gravity acts in the $-y$ direction, similar to the experiment of Pui et al. [15].

4.3.4 Particle parameters

Particles with diameters ranging between 5 - 30 μm are injected (St between 0.05 and 1.35) with a density ρ_p = 895 kg/m^3 and particle-to-fluid density ratio S = 755 similar to Breuer [16]. The number of injected particles is about 15,000 for each Stokes number. Dehbi [13] injected 10,000 particles and found good agreement when comparing the deposition efficiency with the experimental data.

4.3.5 Results

The flow field from the RANS computation in the 90° bend pipe is visualized in Figure 11.a for the velocity field and Figure 11.b for the turbulent kinetic energy.

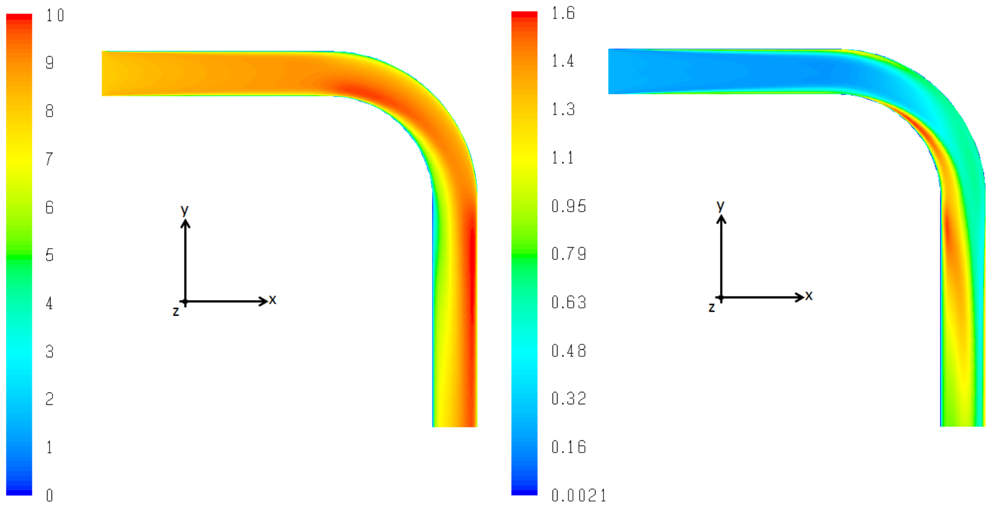

a Velocity magnitude m/s **b** Turbulent kinetic energy m^2/s^2

Figure 11 Flow profiles at midplane of 90° bend pipe.

The obtained deposition efficiency η for the investigated Stokes numbers is shown in Figure 12 in which also the experimental data of Pui et al. [15], the empirical correlation of Pui et al. [15] and the LES results of Breuer [16] are plotted. Also reported is the deposition efficiency result of the LES computation done by NRG which was presented in deliverable D23.51. The overall agreement with the reference data is good albeit a small underprediction in the range of mediate Stokes numbers.

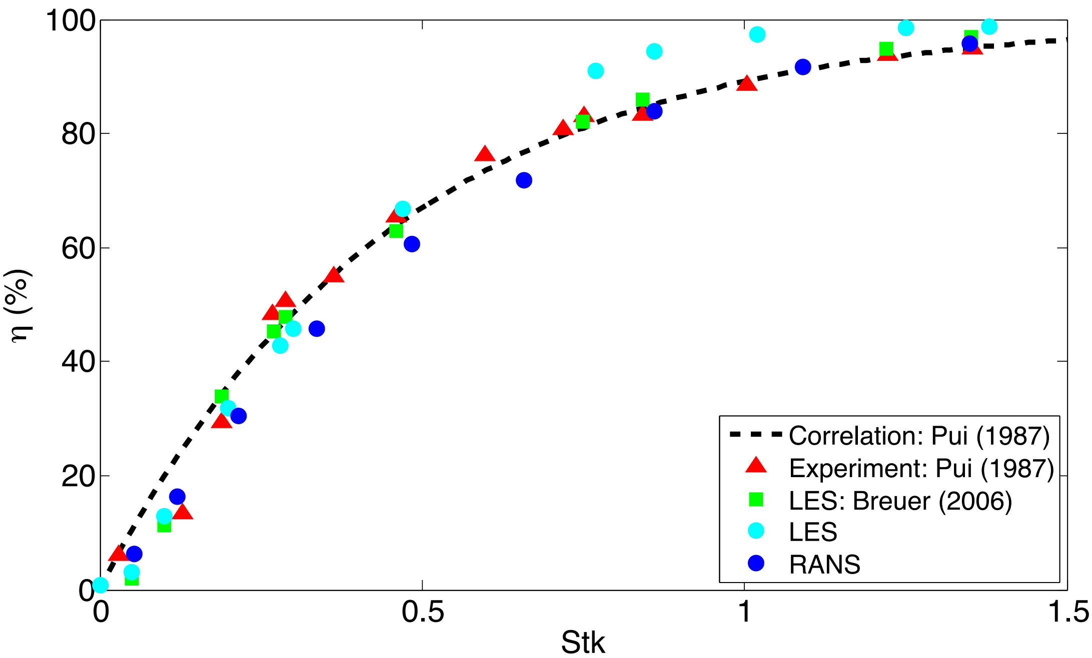

Figure 12   Deposition efficiency η in a 90° bend pipe versus Stokes number. Results of current simulation compared with the experimental data and correlation of Pui et al. [15].

4.4 Spheres

The last case under consideration is particle deposition on a single sphere and an array of spheres.

4.4.1 Experimental data

Hähner et al. [17] and Waldenmaier [18] investigated deposition on spheres experimentally. Waldenmaier used the same set up as Hähner et al. [17]. Deposition on a single sphere as well as on an array of eight spheres was investigated through the experimental facility shown in Figure 13. The monodisperse particles made of DES (Di-II-ethyl-hexyl-sebacate) are injected into the horizontal pipe after initial treatment. The spheres made of steel are located at the center of this horizontal pipe section where the measurements are made. Reynolds numbers between 3,000 and 12,000 were investigated with particle diameters in the range of 1.5 - 15 μm. Particle density is taken to be 915 kg/m^3.

Deposition was reported by means of deposition efficiency defined by:

$$\eta = \frac{M_{dep}}{M_{tot} A u_\infty t} \tag{14}$$

M_{dep} is the mass of deposited particles on the spheres, M_{tot} the total injected mass of the particles, A the projected area of the sphere, u_∞ is the free stream flow velocity and t the collection time.

4.4.2 CFD domain

The computational domains are based on the experiments of Waldenmaier [18]. The spheres have a diameter of 6.5 mm. The two cases, namely the single sphere and the eight spheres array are as shown in Figure 14. In both cases one fourth of the domain is solved applying symmetry conditions. The computational domain starts 7 sphere diameters (D) upstream to allow developed conditions for flow and particles. The domain is extended 7 sphere diameters (D) downstream to ensure no influence of recirculation area on particle deposition on the spheres. For the array of spheres, an inter-sphere spacing of L/D of 1.5 is applied. The domain contains 8 spheres which are aligned in streamwise direction x. Gravity acts in streamwise direction x.

The meshes shown in Figures 15 and 16, are wall-resolved and consists of 0.5 millions cells (single sphere) and 1.1 millions cells (array of 8 spheres).

4.4.3 Flow parameters

Air is used as carrier fluid with density ρ = 1.205 kg/m^3 and viscosity μ = 1.821 $\times$ 10^{-5} Ns/m^2. At the inlet, a velocity of $\bar{U}$ = 13.948 m/s, turbulent kinetic energy of k = 0.849 m^2/s^2 and dissipation rate ω = 3200 m^2/s^3 are applied. The Reynolds number based on the sphere diameter is 6,000.

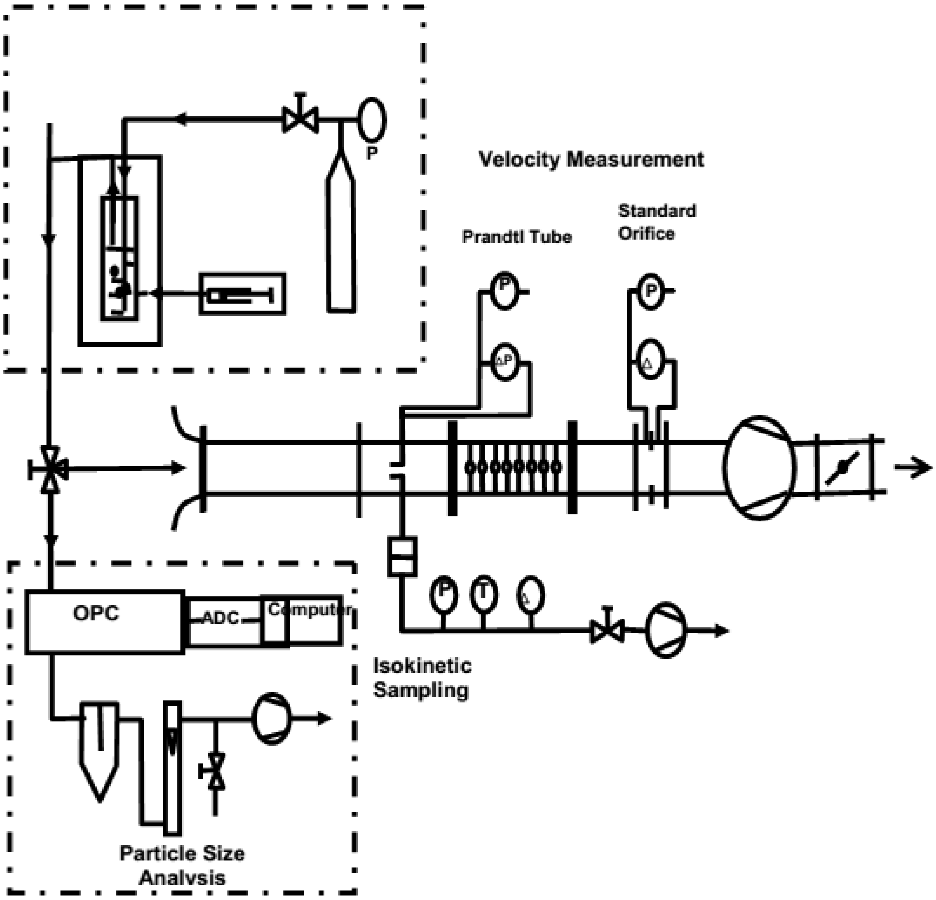

Figure 13 Waldenmaier [18] experimental facility.

4.4.4 Particle parameters

Particles with a diameter in the range of 1 to 16 μm (St = 0.01 to 1.5) are injected. Particle density ρ_p = 915 $\frac{kg}{m^3}$ is equal to the experiments [18].
The injection area is 3 times the sphere diameters in diameter with the center aligned with the center of the sphere(s) in the streamwise direction. In the case with a single sphere, about 30,000 particles are injected in the projected area of the sphere for each particle density. In the case of an array of 8 spheres, about 90,000 particles are injected in the projected area of the sphere for each particle density.
Particle deposition is presented by particle deposition efficiency:

$$\eta = \frac{N_{dep}}{N_{tot}} \tag{15}$$

N_{dep} is the number of deposited particles and N_{tot} is the total number of injected particles.

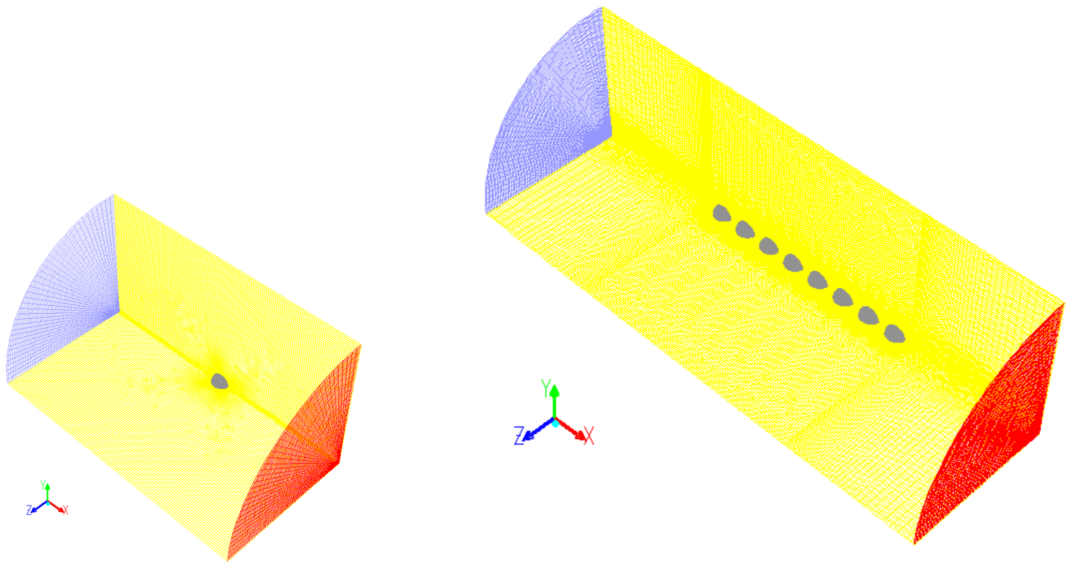

a Single sphere **b** Eight spheres array

Figure 14 Computational domain with single sphere are array of spheres colored by different types of boundaries. inlet(blue); outlet(red); symmetry planes(yellow); spheres wall(grey).

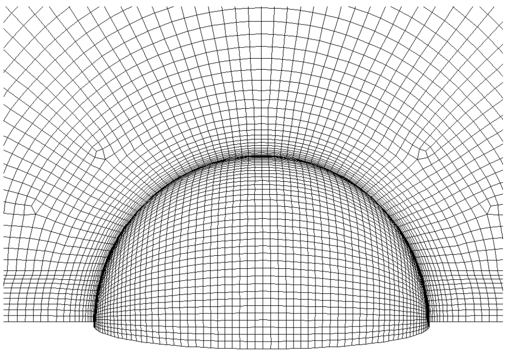

Figure 15 Mesh of single sphere.

4.4.5 Results

In this section the results of simulations with one sphere and with an array are presented. In each configuration, first the resulting flow field is discussed which is followed by a discussion of the results of particle deposition.

Single sphere

The flow fields around the single sphere are as shown in Figure 17. The mean velocity is shown in Fig. 17.a. The flow coming from upstream impinges on the sphere surface to form a stagnation zone in the front and the flow accelerates towards the top. After about 90 degrees, flow separation occurs and a big recirculation zone is formed behind the sphere. The flow kinetic energy is shown in Fig. 17.b. As seen, the maximum

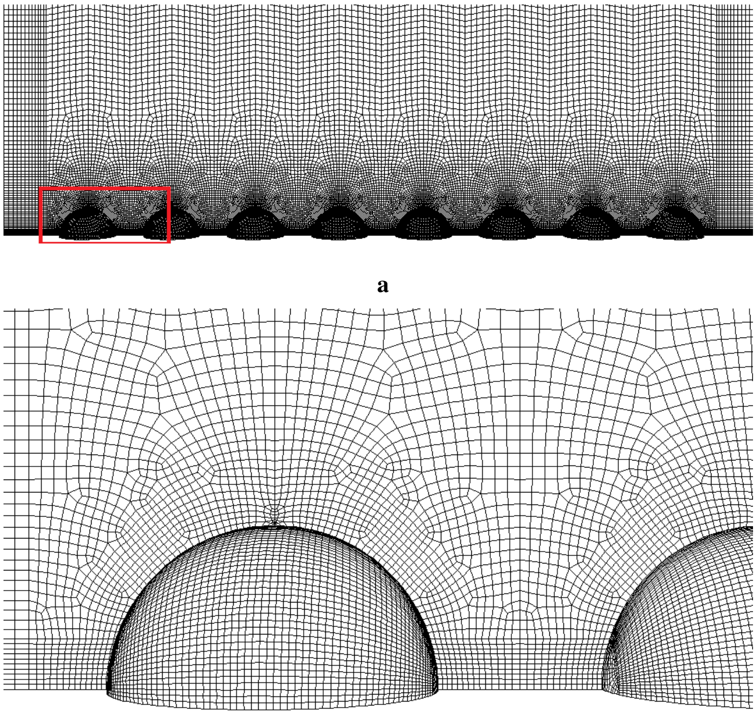

a

b

Figure 16 Mesh of eight spheres array. (a) whole domain; (b) detail of mesh around the spheres.

kinetic energy prevails in the wake region where high velocity gradients are seen.
Figure 18 shows the deposition efficiency as a function of the Stokes number. As seen, the deposition efficiency is in good accordance with experimental results of Waldenmaier et al. [18].

Array of 8 spheres

The flow fields around the array of 8 spheres is displayed in Figure 19. The mean velocity magnitude is as shown in Fig. 19.a. Similar to the single sphere, the flow separation happens at the top of the first sphere. Because of the recirculation zone behing first sphere, most of the flow is directed towards the top surface of rest of the spheres. The recirculation zone prevails in the gaps between all spheres, as well as the last sphere. The flow kinetic energy is shown in Fig. 19.b. As expected, the kinetic energy is generated in the recirculation zones. The maximum value of it is seen in the first recirculation zone formed behind the first sphere and the intensity gradually decreases as we go further downstream.

Figure 20.a and 20.b shows the deposition efficiency for two Stokes numbers of $Stk = 1.2$ and $Stk = 2.3$ respectively. The highest value of deposition efficiency is on the first sphere of the array as the smooth flow upstream of the first sphere ensures maximum sphere area exposed to incoming particles. The maximum difference in deposition prediction on the first sphere is about 5%. Compared to the first sphere, there is a

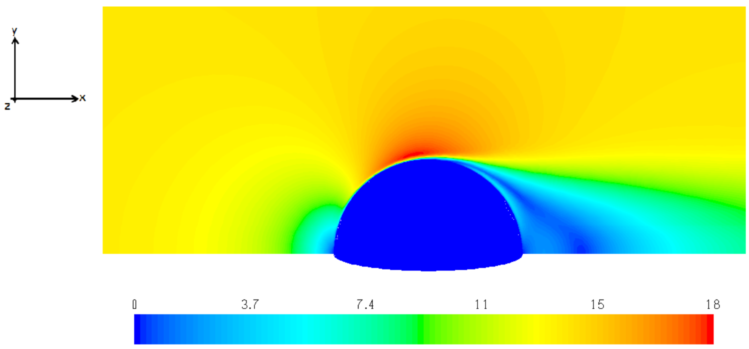

a Velocity magnitude m/s

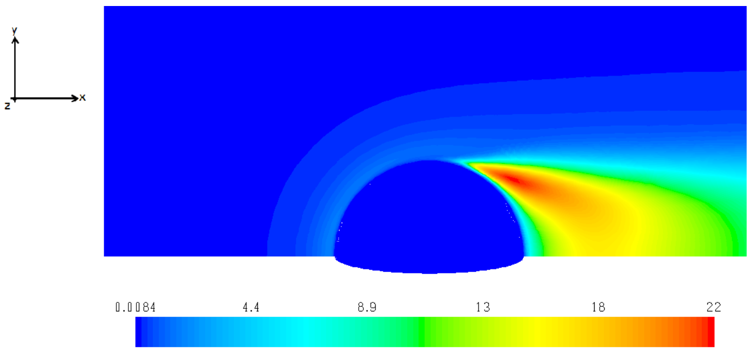

b Turbulent kinetic energy m^2/s^2

Figure 17 Flow field around a single sphere: (a) velocity magnitude; (b) turbulent kinetic energy.

significant drop in the deposition on rest of the spheres. The main reason is that less sphere area is exposed to the incoming flow due to the recirculation zones. The deposition trend of such a significant drop is captured reasonably well by RANS.

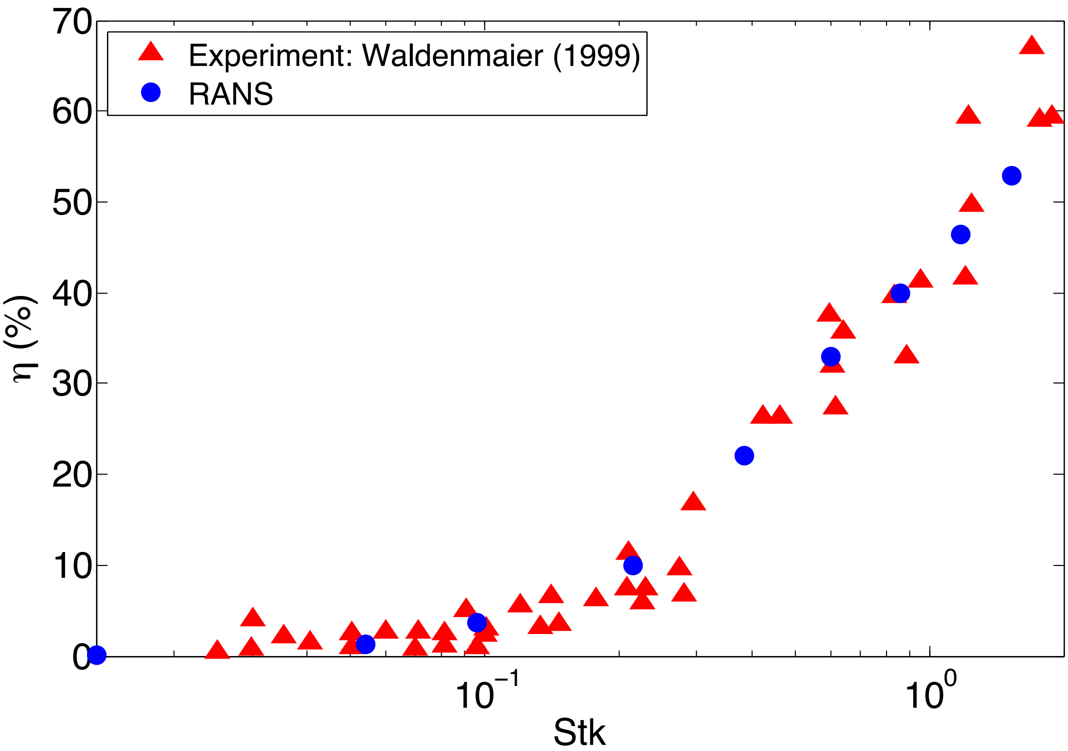

Figure 18 Deposition efficiency η in a single sphere. Results of current simulation compared with the experimental data of Waldenmaier et al. [18]

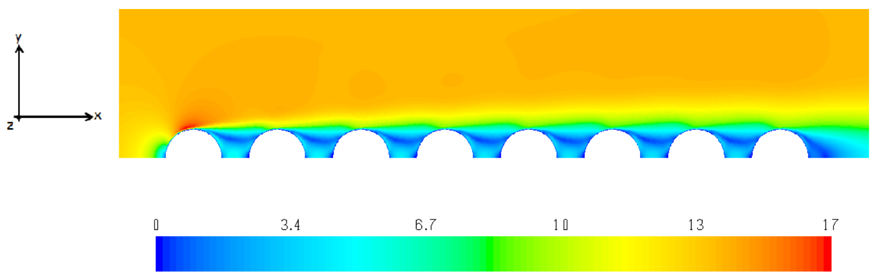

a Velocity magnitude m/s

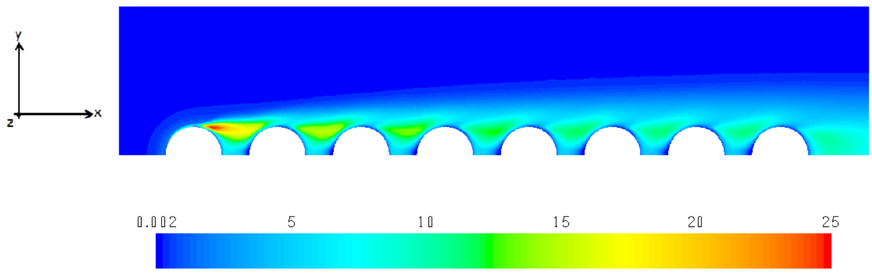

b Turbulent kinetic energy m^2/s^2

Figure 19 Flow field in an array of 8 spheres.

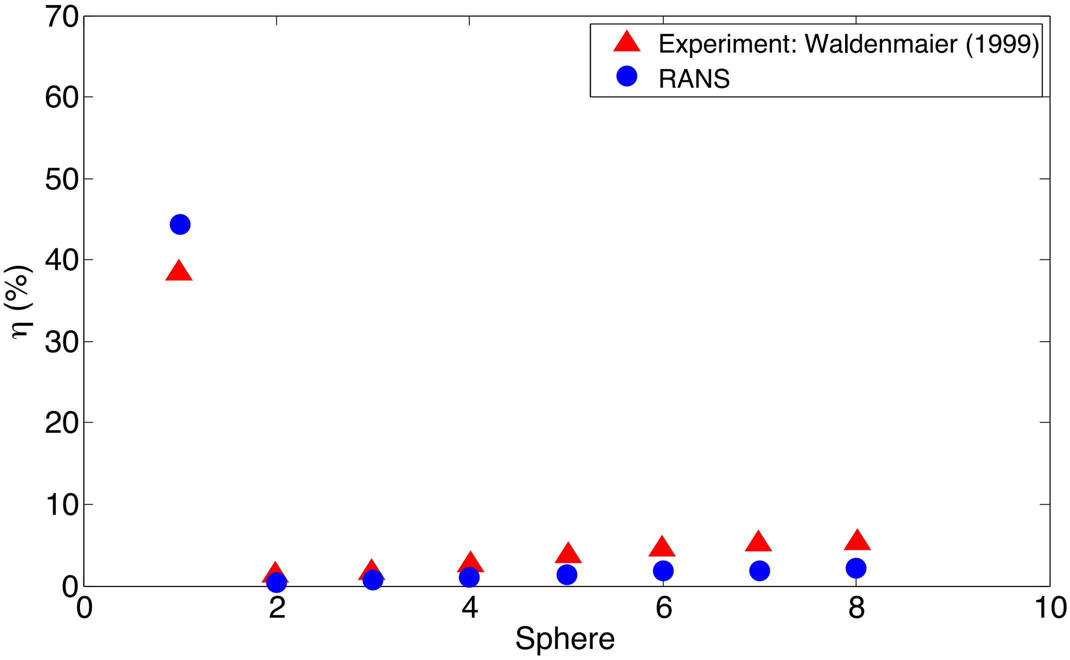

a $Stk = 1.2$

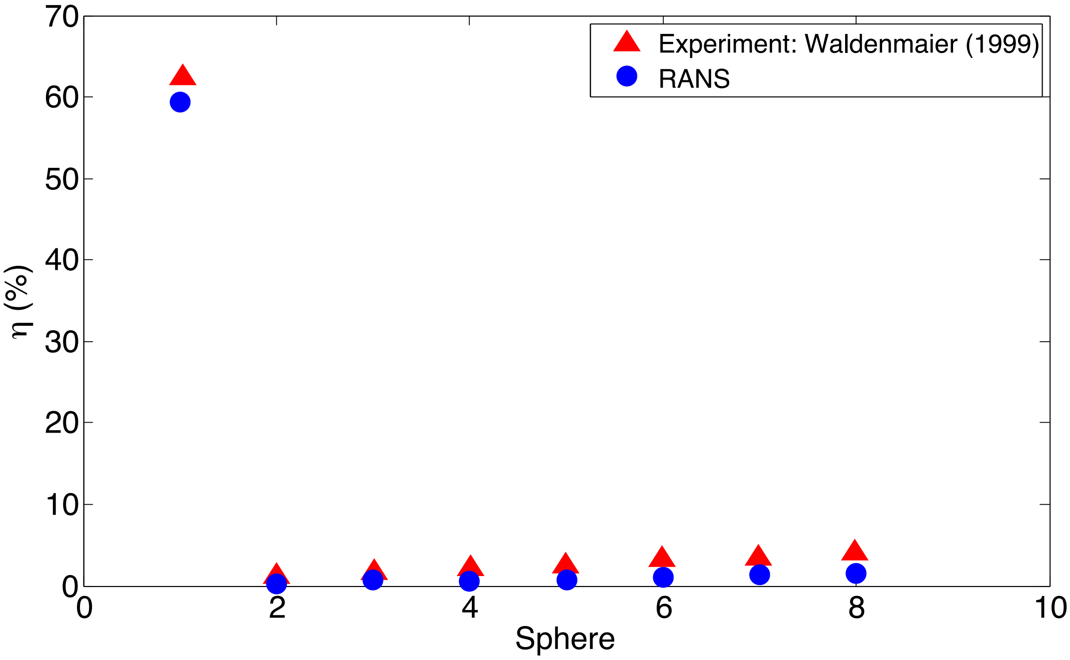

b $Stk = 2.3$

Figure 20 Deposition efficiency η in an array of 8 spheres versus Stokes number. Results of current simulation compared with the experimental data of Waldenmaier et al. [18]

5 Pebble bed specific validation

The previous section has shown generic validation of the modified near-wall anisotropic RANS model for particle transport and deposition. In the present section, this validated model is applied to study complex and realistic cases of particle deposition on pebble beds.

5.1 Experimental data

The flow configuration of a pebble bed has been investigated through experiments and computations. Due to the geometric and measurement complexities, pebble bed experiments performed in the past and even recently have a very limited amount of available data [4]. Recent q-DNS and LES computations of Shams et al. [5],[6],[7] allow more in-depth investigation of the flow structures.

5.2 CFD domain

Three configurations are investigated, two structured pebble beds in face cubic centered (FCC) arrangement and a randomly stacked pebble bed as unstructured geometry.

- A single pebble in face cubic centered (FCC) arrangement is shown in Figure 21.a. By following the specifications of PMBR-250MWth (Lee and Lee, 2010), the diameter of the pebbles is 6 cm. The inter-pebble gap of 5 mm gives a porosity level (ϵ=volume of voids / total volume) of 0.42. The geometry consists of half spherical pebbles at each face and 1/8th at each corner.

- The eight pebbles in face cubic centered (FCC) arrangement is shown in Figure 21.b. The geometrical properties of the spheres respect those of the single pebble in face cubic centered (FCC) arrangement. The geometry consists of 5 half spherical pebbles at each face, 1/8th spherical pebbles at each corner and 1/4th spherical pebbles at each edge.

- A randomly stacked pebble bed arrangement consisting of approximately 30 pebbles with an average porosity level of about 0.4 is given by Pavlidis et al. [19]. The contacts between the pebbles in this arrangement is always a point-contact. To model such point contacts is problematic for meshing and consequently may induce numerical errors. To avoid these difficulties, Shams et al. [6] converted these point contacts into small area contacts by scaling up the pebbles. An up-scaling factor of 1.034 in the LES computation [6]. The porosity would then be slightly smaller than 0.4. In the present work, in order to avoid area contacts altogether, a scaling down is performed on the Pavlidis et al. [19] random arrangement. An small scaling-down factor of 0.966 is applied in the present work for the RANS computation. This results in a over-all porosity to be slightly higher than 0.4. The domain is extended, both on the inlet and the outlet side to avoid developing of turbulent flow towards the inlet region and avoid flow recirculations on the outlet region.

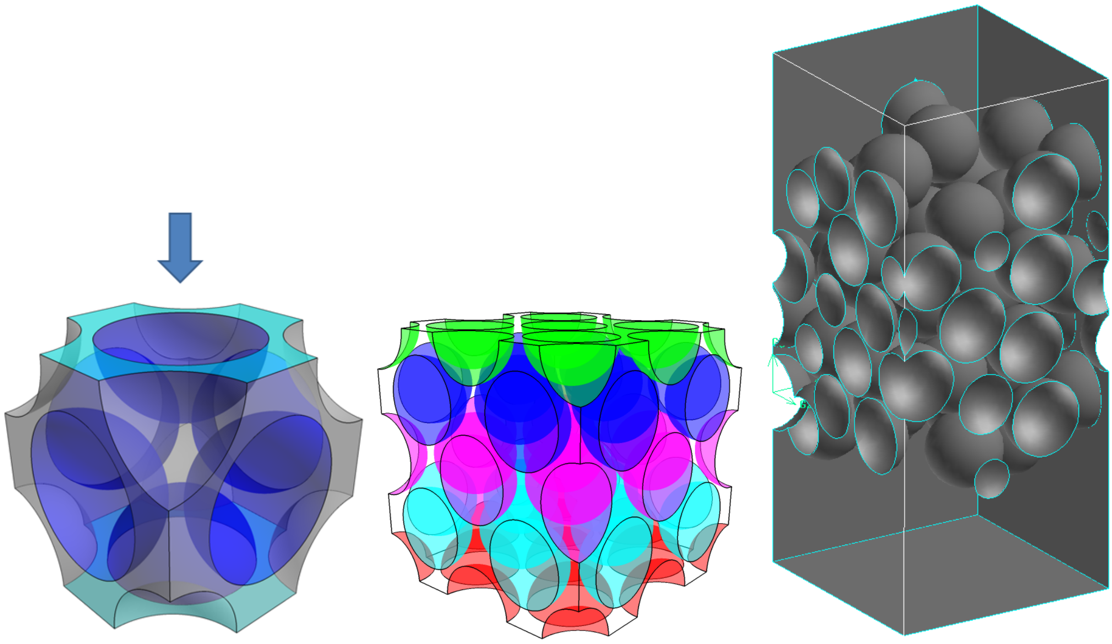

a b c

Figure 21 Computational domain for pebble bed for: (a) single sphere; (b) eight pebbles; (c) randomly stacked eight pebbles.

5.3 Flow parameters

Following a real pebble bed reactor configuration, which is PBMR-250MWth in this study, Helium is considered as a working fluid. The density and viscosity are taken to be 5.36 kg/m^3 and 3.69*10^5 Ns/m^2, respectively at a working temperature and pressure of 773K and 8.5Mpa. A mass flow rate of 0.016 kg/s is used as inlet condition for the single FCC pebble bed. For the eight FCC pebble bed, this mass flow rate was multiplied by four. For the randomly stacked pebble bed is used a velocity inlet of 1.06 m/s. These flow inlet conditions lead to a Reynolds number of 3088 based on the pebble diameter. Based on maximum gap velocity, the estimated Reynolds number appears to be 13,422. The flow direction is always from top to bottom for all three geometries as shown in Fig. 21. Symmetry boundary conditions are applied for the structured cases, walls for the unstructured case. Gravity acts in the flow direction.

5.4 Particle parameters

For the structured FCC cases, injected particles having a diameter in the range of 10 to 300 μm (relaxation time τ^+ = 0.169 to 152) are injected. The particle density is equal to 912 kg/m^3. In the case of a single cubic pebble, about 40,000 particles are injected. In the case of 8 cubic pebbles, about 80,000 particles are injected. For the unstructured case, particles have a diameter in the range of 5 to 300 μm (relaxation time τ^+ = 0.04 to 152) are injected. The particle density is equal to 912 kg/m^3.

The injection area is the total available area at the top of the computational domain.

Particle deposition is presented by particle deposition efficiency:

$$\eta = \frac{N_{dep}}{N_{tot}} \quad (16)$$

N_{dep} is the number of deposited particles and N_{tot} is the total number of injected particles.

5.5 Results

5.5.1 FCC single pebble bed

First of all the flow characteristics are compared with the available q-DNS reference [5]. Flow configuration from RANS results is in good accordance with q-DNS data, as shown in Figure 24. Although the pebbles are arranged in a structured manner, the flow presents a complex topology with peaked velocity and stagnation/separation regions in combination with flow transition. The maximum velocity value is observed through the inter-pebble gap of 5 mm (Figure 22) with formation of high velocity jets. After the narrow inter-pebble gap, the detached jets interact with the recirculation region, which appears downstream of the center half pebble. The interaction causes the subsequent reattachment of the jets. Fluctuations are relatively small in the narrow gaps and in the stagnation regions, however these values reach maxima when the high velocity jet forms a shear layer with the recirculation regions, Figure 23.

Deposition on the top pebbles layer is characterized from direct impact of particles with a low deposition efficiency (Figure 25.a and Figure 26.a). The middle layer is similarly characterized from direct deposition with a uniform particles distribution (Figure 25.b and Figure 26.b). The deposition takes place until the detachment of the velocity boundary layer on the spheres surface. The bottom layer is characterized by non-uniform deposition of particles (Figure 25.b and Figure 26.b) with preferential deposition directions due to the upper pebble layer influence on the flow topology. In Figure 27 is shown the deposition efficiency in function of the non dimensional particle relaxation time for the FCC single pebble bed.

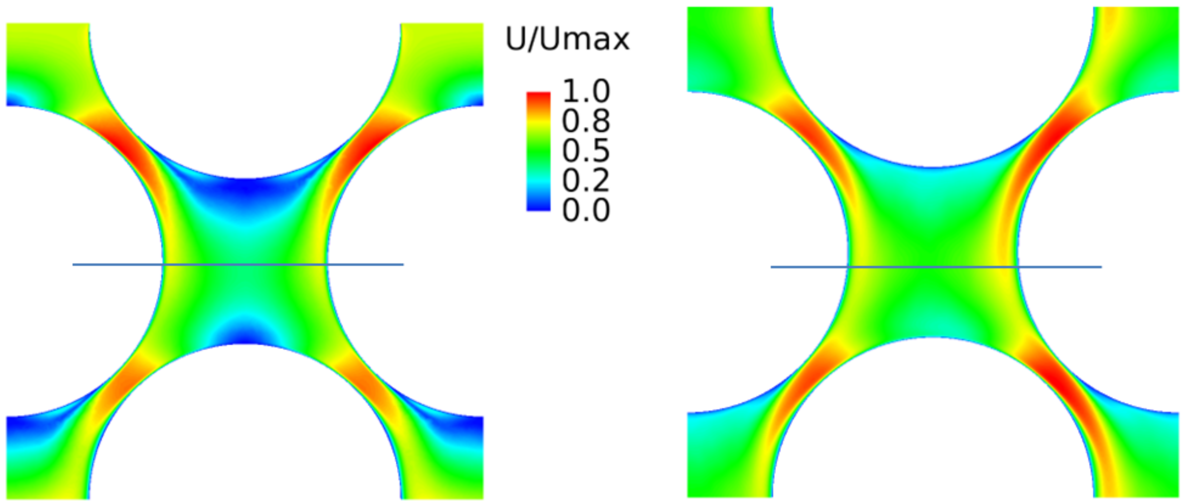

Figure 22   Velocity magnitude for RANS (left) and DNS (right) computation.

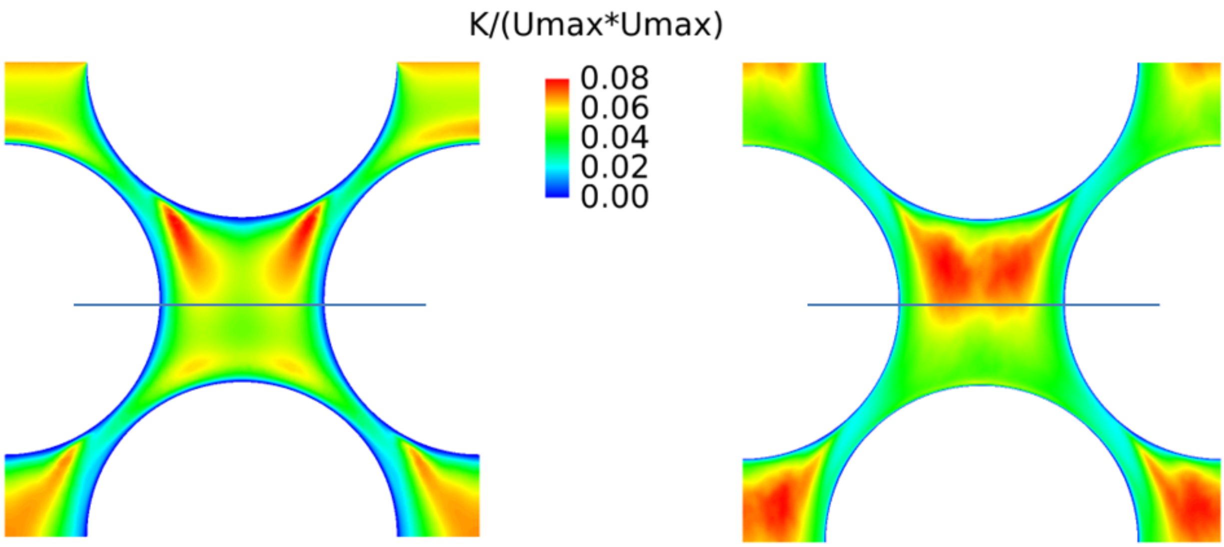

Figure 23   Turbulent kinetic energy for RANS (left) and DNS (right) computation.

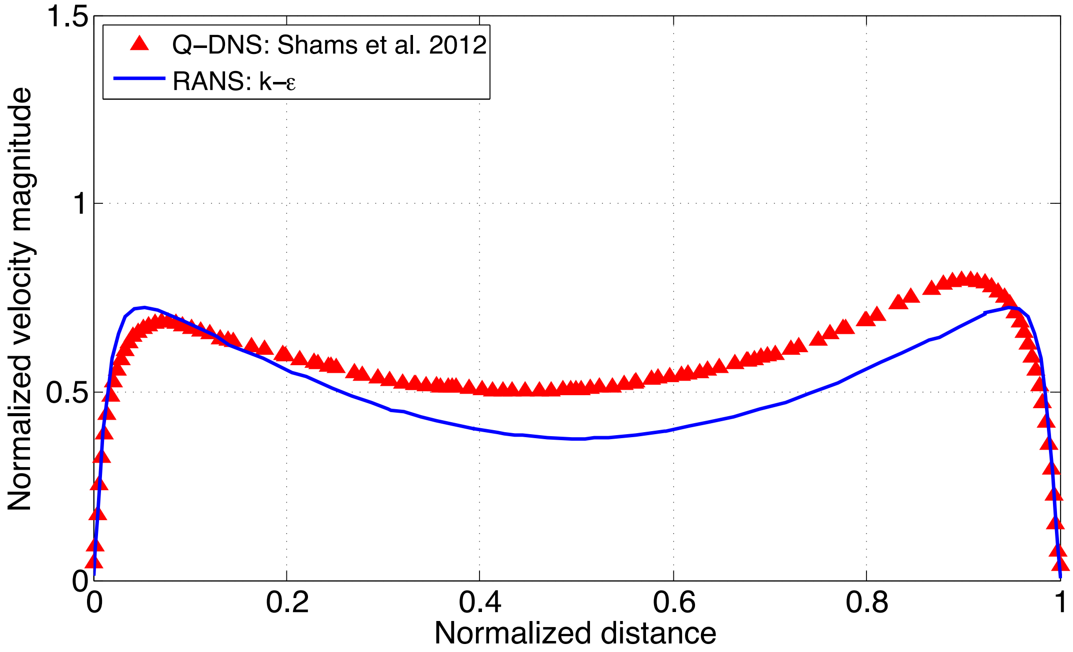

a Velocity magnitude

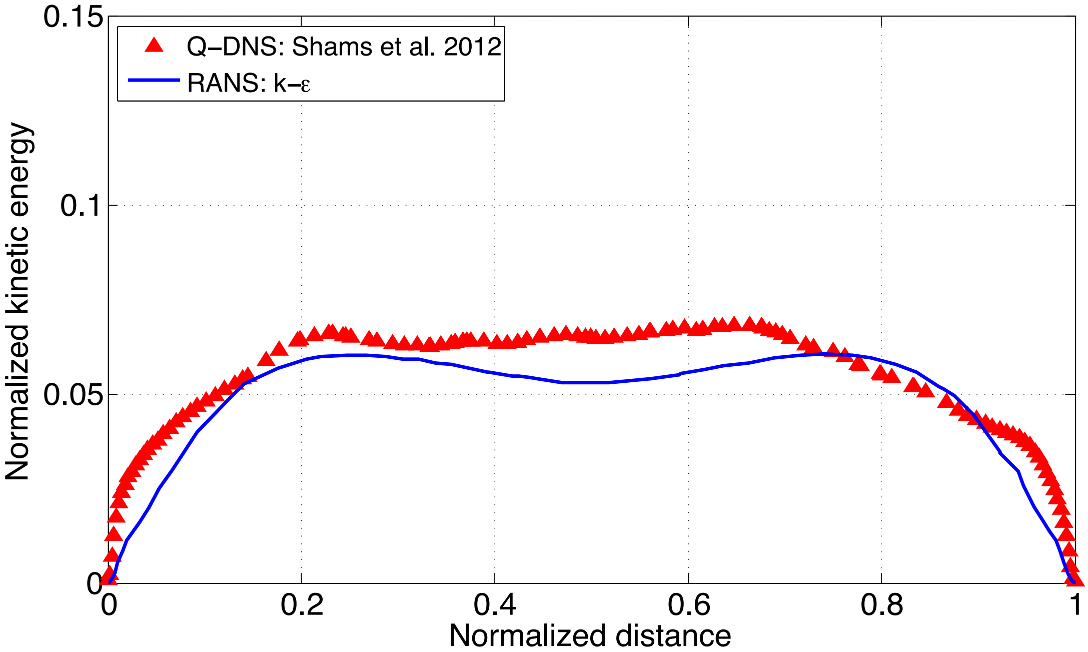

b Turbulent kinetic energy magnitude

Figure 24 Comparison between RANS and DNS results: (a) velocity magnitude; (b) turbulent kinetic energy magnitude.

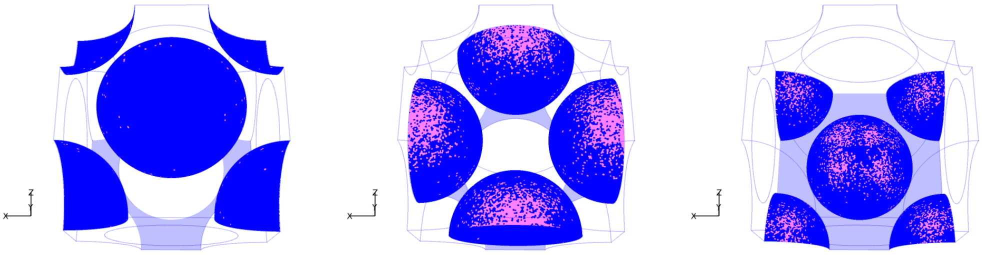

a Top plane **b** Middle plane **c** Bottom plane

Figure 25 Particle deposition, $d_P = 50\ \mu m$, $\tau^+ = 4.2$.

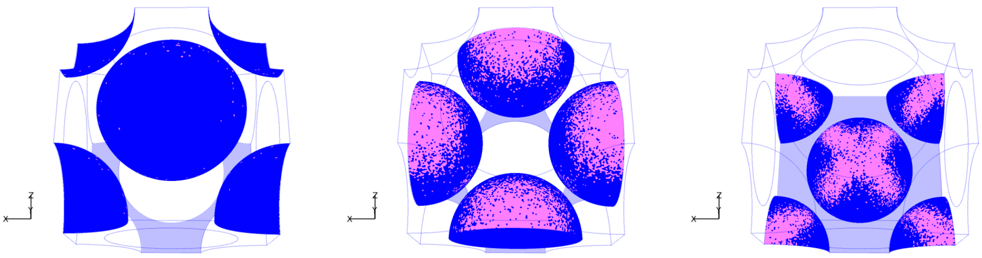

a Top plane **b** Middle plane **c** Bottom plane

Figure 26 Particle deposition, $d_P = 100\ \mu m$, $\tau^+ = 16.9$.

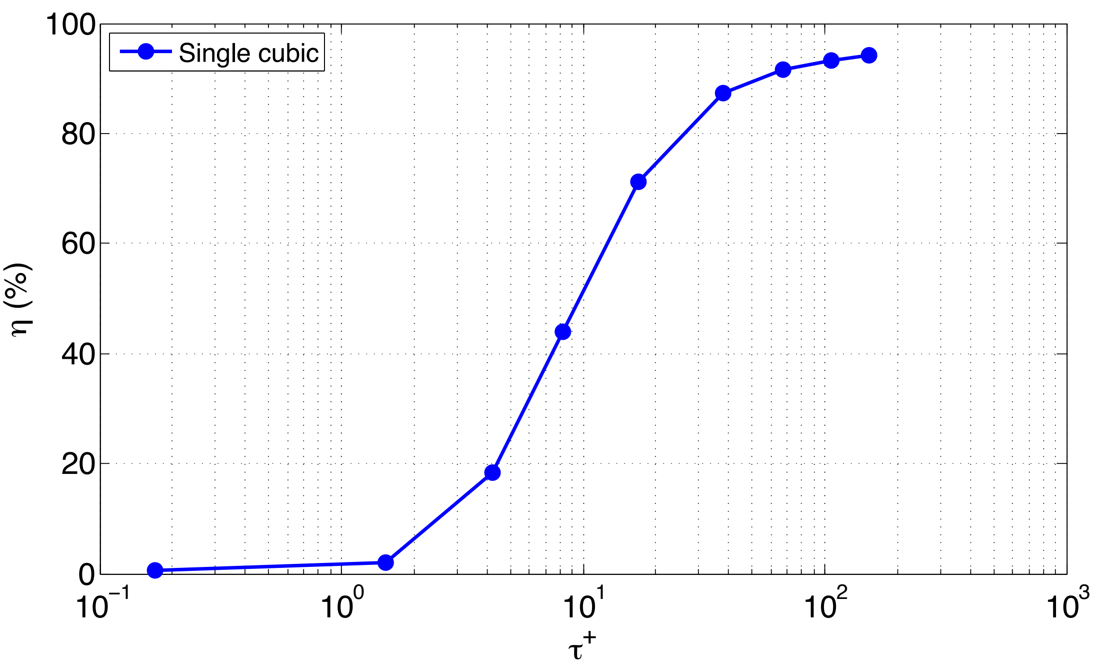

Figure 27 Deposition efficiency for single pebble bed.

5.5.2 FCC eight pebble bed

The flow configuration for a FCC eight cubic pebble bed, as shown in Figure 28, shows similarities with the single pebble bed geometry. The velocity magnitude and turbulent kinetic energy peaks are observed through the inter-pebble gap, related to the presence of high velocity jets. Two different stagnation regions are observed, similarly to the single pebble bed case: one on the front and one on the back of the pebbles.

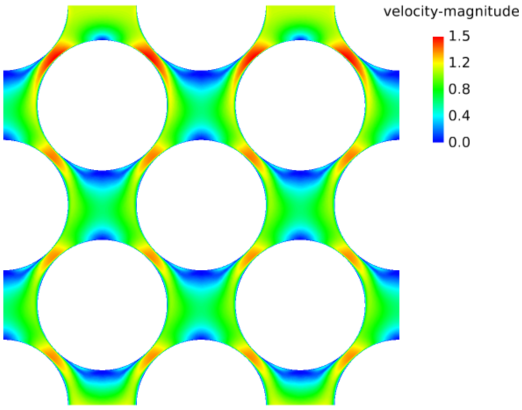

a Velocity magnitude

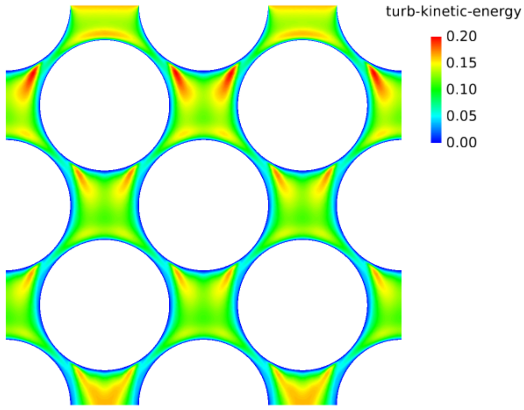

b Turbulent kinetic energy magnitude

Figure 28 Fields comparison: (a) velocity magnitude; (b) turbulent kinetic energy magnitude.

The particle deposition takes place in a similar way as with the single pebble bed case. The first layers are characterized from direct impact of particles (Figure 29.a, 29.b and Figure 30.a, 30.b). The lower layers are showing deposition effected from the non homogeneous flow configuration,(Figure 29.c, 29.d, 29.e and Figure 30.c, 30.d, 30.e). In Figure 31 is shown the deposition efficiency for both FCC geometries. The deposition efficiency fot the eight FCC pebble bed is higher than the single FCC pebble bed because of the higher impact surface available.

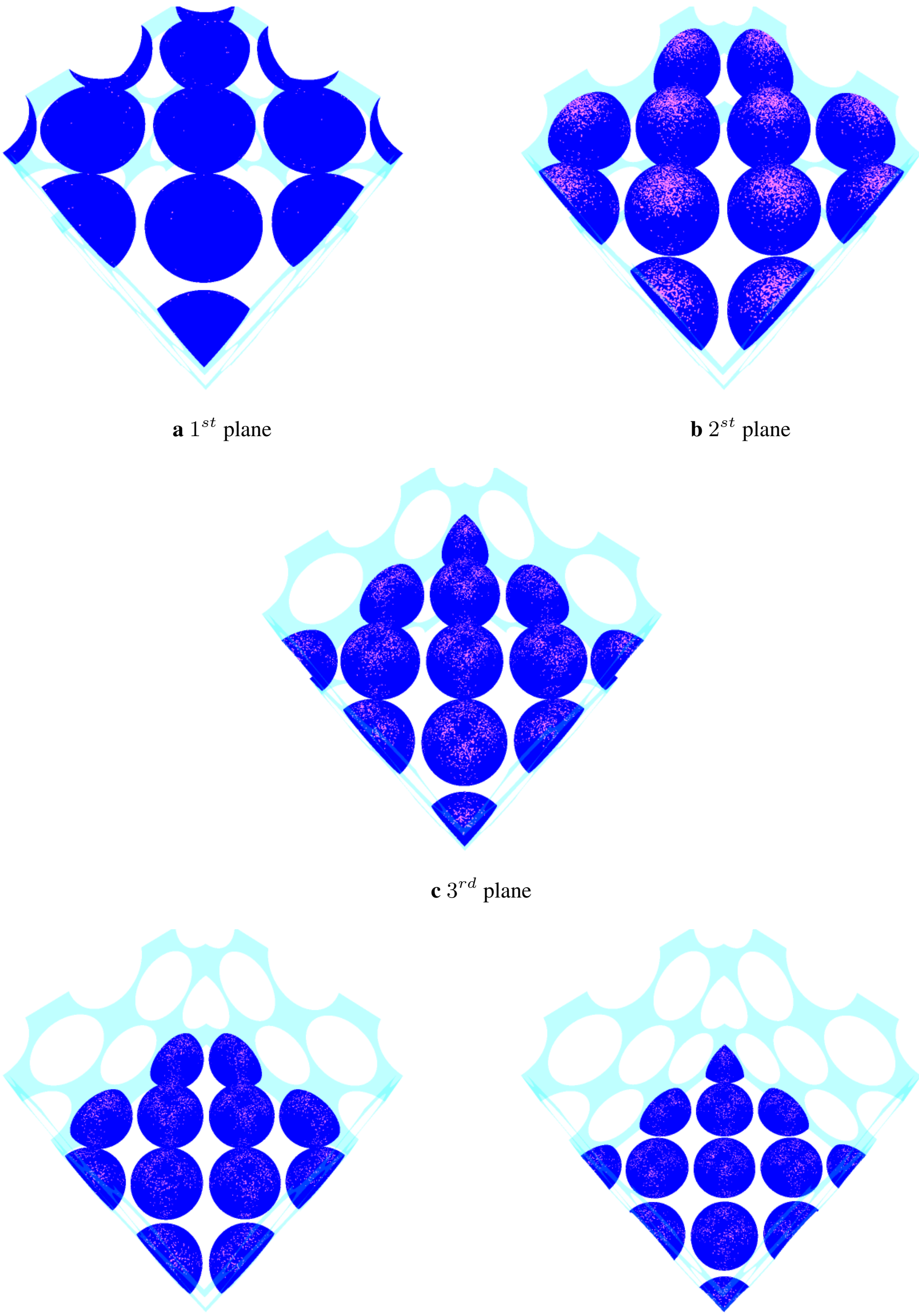

a 1^{st} plane **b** 2^{st} plane **c** 3^{rd} plane **d** 4^{th} plane **e** 5^{th} plane

Figure 29 Particle deposition, $d_P = 50\ \mu m$, $\tau^+ = 4.2$.

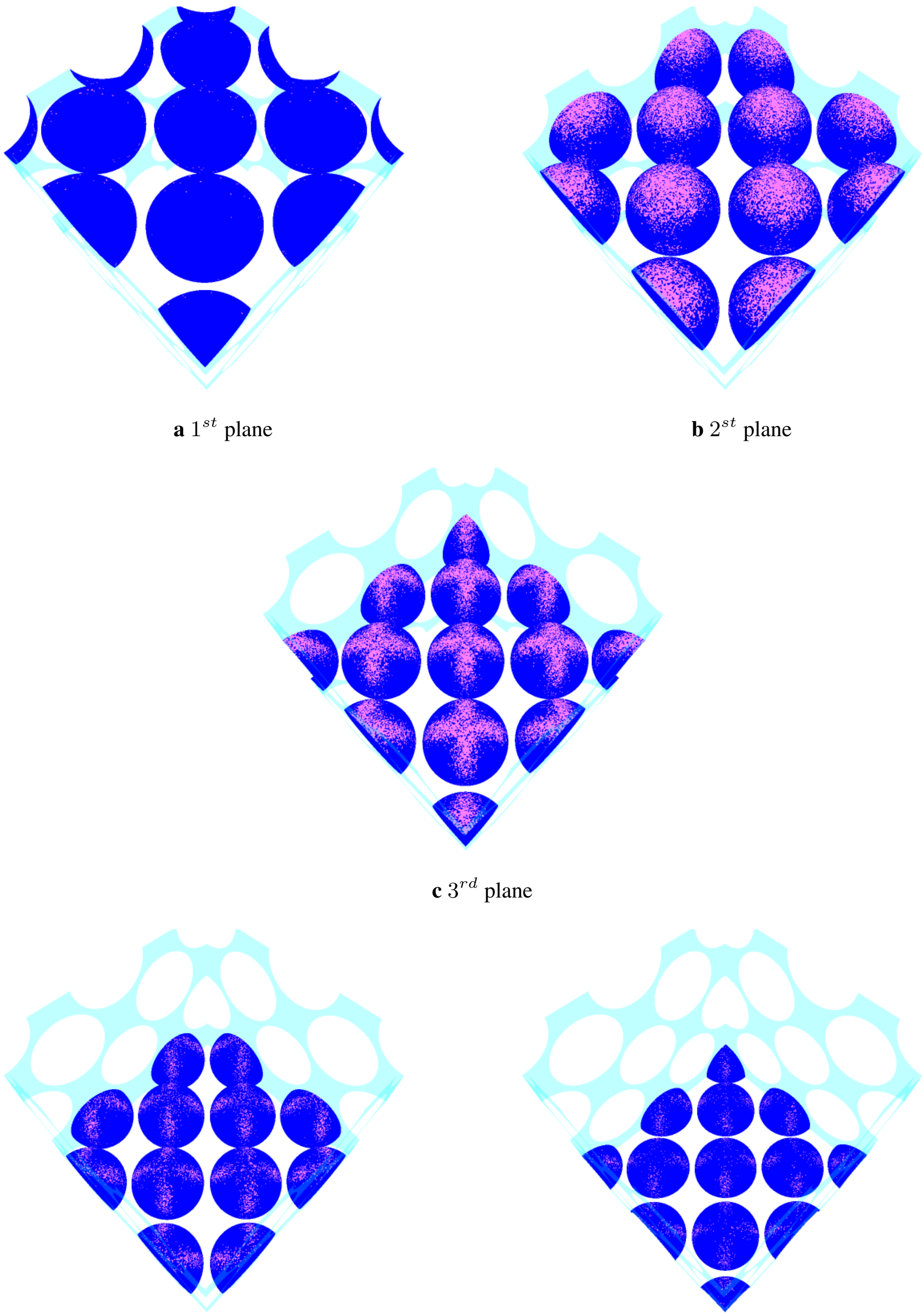

a 1^{st} plane **b** 2^{st} plane **c** 3^{rd} plane **d** 4^{th} plane **e** 5^{th} plane

Figure 30 Particle deposition, $d_P = 100\ \mu m$, $\tau^+ = 16.9$.

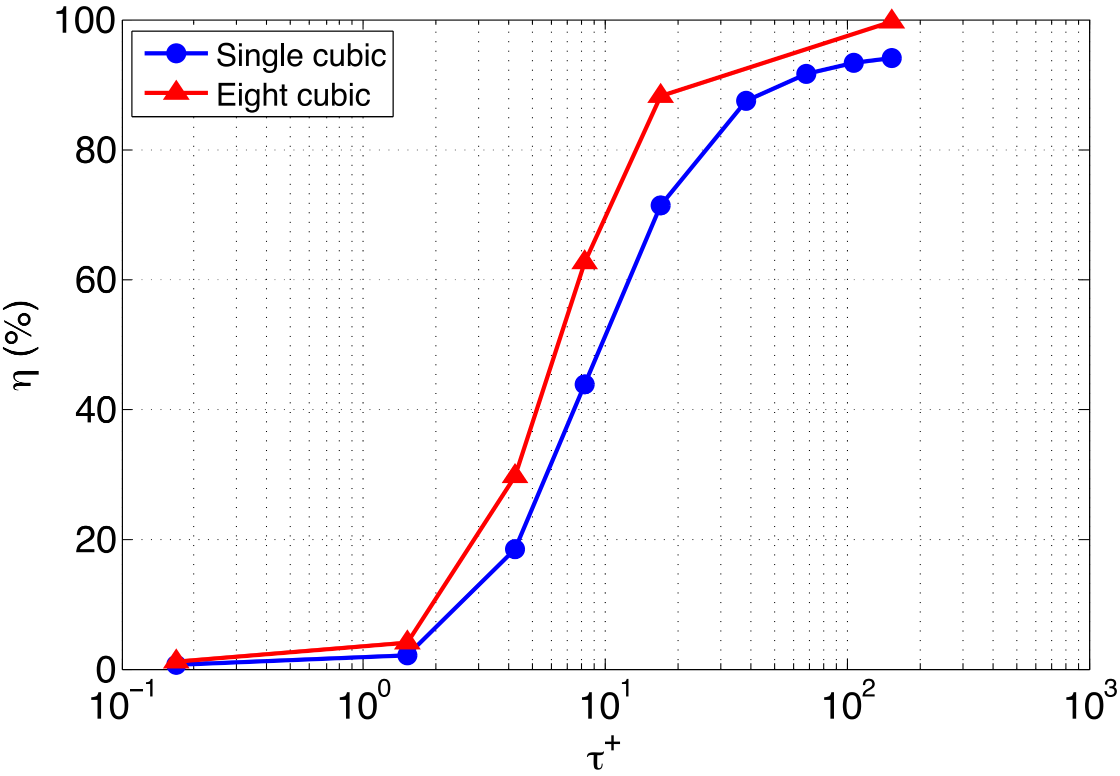

Figure 31   Deposition efficiency: single and eight spheres pebble bed.

5.5.3 Randomly stacked eight pebble bed

Again, the generic flow characteristics are first compared to the reference data from Shams et al. [6]. The velocity magnitude is shown in Figure 32.a and Figure 32.b. The turbulent kinetic energy is shown in Figure 33.a and Figure 33.b. The random disposition of pebbles induces a random and highly complex flow topology, although flow structures are observed similar to flow structures appearing in the structured eight pebble bed.

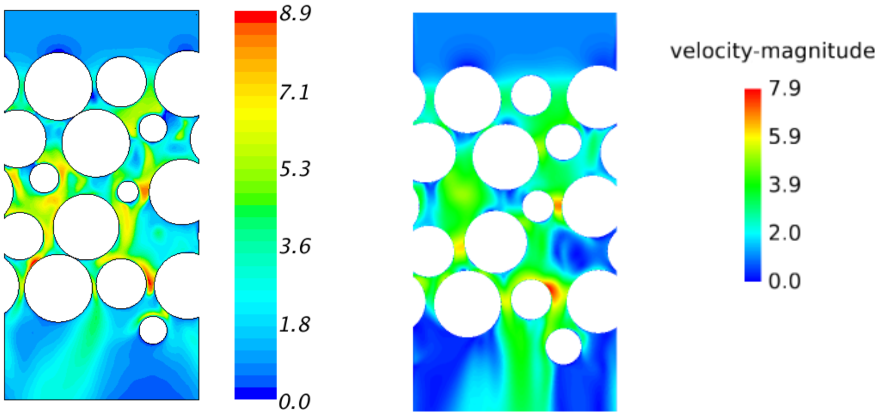

b LES **a** RANS

Figure 32 Velocity magnitude in a z normal plane: LES result (left) and RANS result (right).

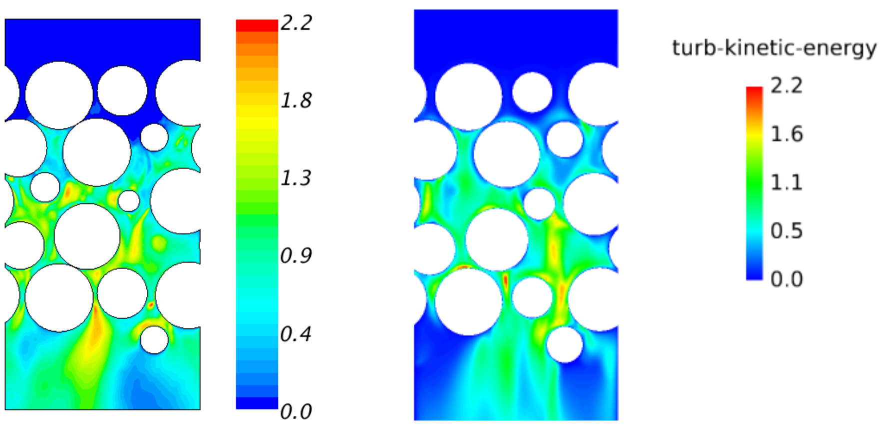

a LES **b** RANS

Figure 33 Turbulent kinetic energy magnitude in a z normal plane: LES result (left) and RANS result (right).

The complex nature of the case leads also to a complex deposition of particles as can be seen in Figure 34. The deposition efficiency is shown in Figure 35. This is higher than in the structured cases. This is probably related to the complex flow topology, where the interaction between high velocity flow streams through inter-pebble gaps increases the impacting particles on the pebbles surfaces. Furthermore, the lower inlet flow rate (compared to the structured cases) increases the particles residence time, increasing the probability of particle deposition principally at low Stokes number.

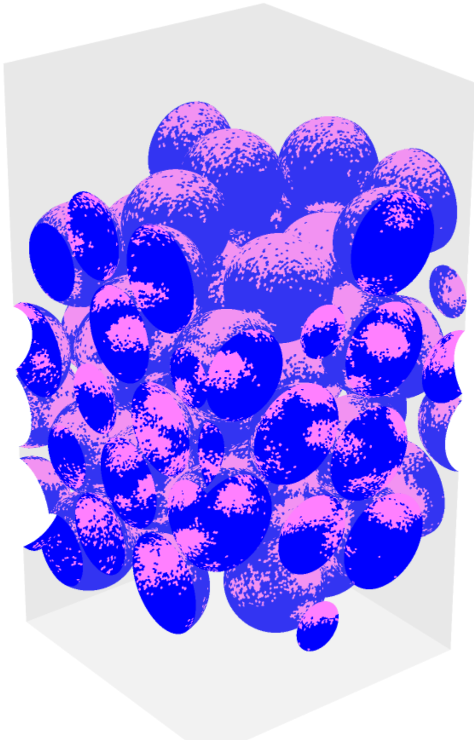

Figure 34 Particle deposition, $d_P = 100\ \mu m$

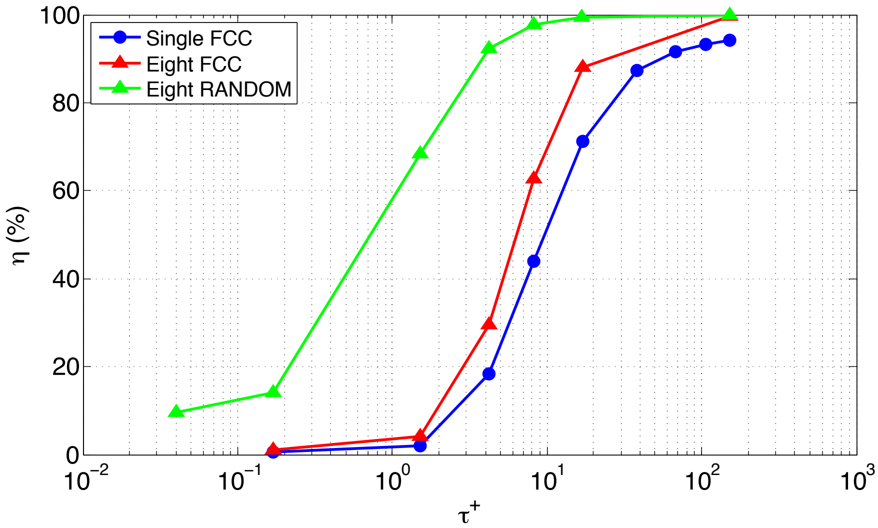

Figure 35   Deposition efficiency.

6 Conclusions

The first deliverable D23.51 was related to generic validation for the RANS and LES CFD approaches to predict the particle transport and deposition. Detailed literature review was performed to collect and evaluate the available experimental and Direct Numerical Simulation (DNS) data pertaining to the particle deposition validation. In case of RANS modelling, several uncertainties regarding the near-wall modeling were addressed. A robust and well validated RANS model coupled with a specific near-wall correlation was proposed for the accurate particle transport and deposition predictions. Additionally, the capability of a more advanced model such as the LES was validated by performing two test cases.

The present deliverable D23.52 concerns the application of the validated model presented in D23.51 to perform pebble-bed specific validation. Due to the geometric and measurement complexities, random pebble bed experiments performed in the literature have a very limited amount of available data. The recent experiments from [4] provide good quantitative predictions of particle deposition behavior in a randomly stacked pebble beds, however, no explicit data is available to translate the random pebble bed arrangement into a CAD model. Due to such limitations, it becomes difficult to directly apply the proposed model in D23.51 to predict particle transport and deposition in complex domains of random pebble beds. Hence, the proposed model in D23.51 is further validated in the present work by applying it to simple cases such as duct flow, straight pipe flow and bend pipe flow where experimental data were available for particle deposition. Good agreement in deposition patterns were seen for all these cases. In the second stage, the proposed model is further validated by applying it to cases such as flow over a single sphere and flow over array of spheres where experimental data were available for particle deposition. These validation cases more resemble the complex flow which can be expected in pebble-beds. Reasonably good agreement in deposition patterns were observed for these two cases. The aforementioned validations provided a robust and well-validated particle transport and deposition model which could be further used for predicting particle deposition in pebble-beds.

The model was further applied to study particle deposition in two structured pebble beds in face cubic centered (FCC) arrangement and a random-pebble bed arrangement. From fluid flow point of view, recent q-DNS and LES computations of Shams et al. [7] allowed more in-depth validation of the flow structures. From particle transport and deposition perspective, these cases enabled us to systematically demonstrate the deposition patterns in such arrangements.

References

[1] S T Jayaraju, P Sathiah, and H Bijleveld. Generic validation of RANS and LES CFD approaches against existing DNS database. ARCHER project deliverable D23.51, Nuclear Research and Consultancy Group, 2014.

[2] M P Kissane, F Zhang, and M W Reeks. Dust in HTRs: Its nature and improving prediction of its resuspension. *Nuclear Engineering and Design*, 251:301–305, 2011.

[3] M P Kissane. A review of radionuclide behaviour in the primary system of a VHTR. *Nuclear Engineering and Design*, 239:3076–3091, 2009.

[4] J. Kulenkampf M. Grndigb K. Franke J. Lippmann-Pipke U. Hampela T. Barth, M. Ludwig. Positron emission tomography in pebble beds. part 1: Liquid particle deposition. *Nuclear Engineering and Design*, (In press), 2013.

[5] E.M.J. Komen E. Baglietto A. Shams, F. Roelofs. Quasi-direct numerical simulation of a pebble bed configuration. part i: Flow (velocity) field analysis. *Nuclear Engineering and Design*, 263:473–489, 2013.

[6] E.M.J. Komen A. Shams, F. Roelofs and E. Baglietto. Large eddy simulation of a randomly stacked nuclear pebble bed. *Computer and fluids*, 96:302–321, 2014.

[7] E.M.J. Komen A. Shams, F. Roelofs and E. Baglietto. Calibration of a pebble bed configuration for direct numerical simulation. *Nuclear Engineering and Design*, 242:331–340, 2012.

[8] G Lecrivain and U Hampel. Influence of the Lagrangian integral time scale estimation in the near wall region on particle deposition. *Journal of Fluids Engineering*, 134(7), 2012.

[9] Matthias Reiche Thomas Barth, Jakob Preuss and Uwe Hampel. Gas/graphite flow: Single and multilayer particle resuspension experiments in turbulent channel flows. *2nd THINS Cluster Workshop - Stockholm, KTH*, February 6-7, 2013.

[10] N.B. Wood. A simple method for the calculation of turbulent deposition to smooth and rough surfaces. *Journal of Aerosol Science*, 12:275–290, 1981.

[11] L Tian and G Ahmadi. Particle deposition in turbulent duct flows - comparison of different model predictions. *Journal of Aerosol Science*, 38:377–397, 2007.

[12] B Y H Liu and J K Agarwal. Experimental observation of aerosol deposition in turbulent flow. *Journal of Aerosol Science*, 5-2:145–158, 1974.

[13] A. Dehbi. Turbulent particle dispersion in arbitrary wall-bounded geometries: A coupled cfd-langevin-equation based approach. *International Journal of Multiphase Flow*, 34:819–828, 2008.

[14] D D McCoy and T J Hanratty. Rate of deposition of droplets in annular two-phase flow. *International Journal of Multiphase Flow*, 3:319–331, 1977.

[15] D Y H Pui, F R Novas, and B Y H Liu. Experimental study of particle deposition in bends of circular cross section. *Aerosol Science and Technology*, 7-3:301–315, 1987.

[16] M Breuer. A challenging test case for large eddy simulation: High reynolds number circular cylinder flow. *International Journal of Heat and Fluid Flow*, 21(5):648–654, 2000.

[17] Hähner et al. Inertial impaction of aerosol particles on single and multiple spherical targets. *Chemical Engineering Technology*, 17:88–94, 1994.

[18] Matthias Waldenmaier. Measurements of inertial deposition of aerosol particles in regular arrays of spheres. *Journal of Aerosol Science*, 30 (10):1281–1290, 1999.

[19] D Pavlidis and D Lathouwers. Realistic packed bed generation using small numbers of spheres. *Nuclear Engineering and Design*, 263:172–178, 2013.